An Omnidirectional Wireless Power Transfer System via Two Orthogonal Bipolar Coils and Targeting Magnetic Field Control for UAVs

Tianxu Feng, *Member, IEEE*, Yuxuan Xu, Jincheng Jiang, Ke Shi, *Member, IEEE*, Peiyue Wang,
and Jie Hou, *Member, IEEE*

***Abstract*—Misalignment tolerance represents a critical challenge in uncrewed aerial vehicle wireless power transfer (UAV-WPT) systems. Conventional approaches enhance positional and angular misalignment tolerance by generating wide-range omnidirectional magnetic fields through transmitter design or rotating field techniques. However, these methods exhibit a low magnetic field utilization rate since UAVs typically require only specific field orientations postlanding rather than omnidirectional fields. This article proposes a UAV-WPT system employing two orthogonal bipolar transmitting coils with a targeting magnetic field to achieve omnidirectional powering and enhance the magnetic field utilization rate simultaneously. COMSOL simulations are used to analyze the magnetic field distribution of the transmitter, and the principles for generating a targeting magnetic field through excitation current control are explained. The amplitude and phase of the excitation currents are controlled by adjusting the duty cycle and phase difference of the two half-bridge inverters. The mathematical relationships between maximum output power, maximum input power, and maximum transmission efficiency with respect to duty cycle and phase difference are established. A targeting magnetic field control method combining phase difference and duty cycle scanning is proposed. Experimental results show that the system can establish a targeting magnetic field within 85 ms, with a maximum output power of 216.2 W and a peak dc-to-dc efficiency of 89.5%. The dc-to-dc efficiency exceeds 76.1% across ±100 mm positional misalignment and arbitrary angular misalignment. The dc-to-dc efficiency of the targeting magnetic field mode is at least 5% higher than that of the rotating magnetic field mode.**

***Index Terms*—Misalignment tolerance, omnidirectional, targeting magnetic field, uncrewed aerial vehicles (UAVs), wireless power transfer (WPT).**

I. Introduction

UNCREWED aerial vehicles (UAVs), characterized by their flexibility, efficiency, and safety, offer significant advantages for a diverse range of applications, such as military, agriculture, power inspection, environmental monitoring, logistics delivery, and disaster rescue [1], [2], [3]. Wireless power transfer (WPT) technology enables autonomous replenishment for UAVs, significantly extending operational range and facilitating unattended operations. This technology is pivotal for advancing the overall intelligence of the UAV systems [4], [5].

The face-to-face circular or rectangular coil structures represent the predominant magnetic coupler topology in UAV-WPT systems [6], [7], [8], [9], [10]. However, mounting circular or rectangular receivers in face-to-face arrangements on the belly of a UAV will destroy the overall shape and structure of the UAV, obstruct the view below the UAV, increase flight resistance, and increase leakage flux interference on UAV equipment. Consequently, the face-to-face magnetic couplers have poor structural compatibility for UAV-WPT applications. To meet the requirement of structural compatibility, a three-phase tightly coupled mechanism is proposed in [11], an orthogonal magnetic structure is developed in [12], and two orthogonal transmitters with double L-type ferrite are designed in [13]. However, these magnetic couplers have poor tolerance to positional and angular misalignment.

Considering the requirement of omnidirectional powering for UAVs, a target-shaped transmitter is proposed in [14], an asymmetric magnetic coupler is introduced in [15], a transmitter consisting of one inner circular coil and one outer coil is designed in [16], an embedded lightweight squirrel-cage receiver is explored in [17], and a bipolar four-coil structure and a four-solenoid receiving structure is proposed in [18]. All these transmitters can generate omnidirectional magnetic fields in the horizontal plane. However, each transmitter contains only a single transmitting coil, rendering them incapable of controlling magnetic field direction through magnetic field vector superposition. In practice, once a UAV completes its landing, its position and angle typically remain fixed. When the receiver maintains a stationary position and angle, only a magnetic field with a specific orientation is required, not an omnidirectional field. Because continuous generation of omnidirectional magnetic fields will reduce magnetic field utilization rate.

Received 23 July 2025; revised 30 September 2025; accepted 31 October 2025. Date of publication 4 November 2025; date of current version 19 January 2026. This work was supported in part by the National Natural Science Foundation of China under Grant 52307004 and Grant 62373070, in part by the Chongqing Natural Science Foundation under Grant CSTB2024NSCQ-MSX0667 and Grant CSTB2024NSCQ-QCXMX0054, and in part by the Science and Technology Research Program of Chongqing Municipal Education Commission under Grant KJQN202500615 and Grant KJQN202400626. Recommended for publication by Associate Editor K. Ngo. *(Corresponding author: Jincheng Jiang.)*

The authors are with the School of Automation, Chongqing University of Posts and Telecommunications, Chongqing 400065, China (e-mail: fengtx@cqupt.edu.cn; s240331105@stu.cqupt.edu.cn; jiangjinc@cqupt.edu.cn; shike@cqupt.edu.cn; wangpy@cqupt.edu.cn; houjie@cqupt.edu.cn).

Color versions of one or more figures in this article are available at https://doi.org/10.1109/TPEL.2025.3628890.

Digital Object Identifier 10.1109/TPEL.2025.3628890

Multiple transmitting coils with magnetic field control are a possible solution to improve magnetic field utilization rate. Cai et al. [19] proposed a combined square and dipole transmitter that can generate a rotating magnetic field to improve the angular misalignment capability. Wu et al. [20] proposed a free-positioning UAV-WPT system via a reconfigurable coil array and a rotating magnetic field. Zhang et al. [21] established a dynamic magnetic field based on two-phase transmitting circular coils arranged at intervals to achieve omnidirectional charging for UAVs. Cai et al. [22] designed a UAV wireless charging platform featuring a reconfigurable array capable of generating an omnidirectional rotating magnetic field. The above approaches excite two-phase coils with 90° phase difference currents or three-phase coils with 120° phase difference currents to generate 2-D rotating magnetic fields. These rotating magnetic fields exhibit temporally varying orientations that can point in all directions in a 2-D plane. Using a rotating magnetic field to achieve omnidirectional powering has the advantages of not requiring receiver angle detection and being simple to implement. However, this method suffers from low magnetic field utilization rate. Because during a full scanning cycle of the rotating magnetic field, only during brief intervals is the generated magnetic field perpendicular to the receiving coil plane. For the majority of the cycle, the produced magnetic flux remains unusable by the receiving coil. Generally, enhancing magnetic field utilization rate is desirable to reduce flux leakage and improve power transfer efficiency. However, present UAV-WPT systems rarely satisfy both omnidirectional powering and high magnetic field utilization rate requirements simultaneously.

To this end, this article proposes a targeting magnetic field control method for a UAV-WPT system to achieve omnidirectional powering and a high magnetic field utilization rate. The transmitter comprises two orthogonal bipolar coils, each driven by a half-bridge inverter. The receiver incorporates two rectangular coils coplanar with the UAV landing gear. The two transmitting coils predominantly generate x-directional and y-directional magnetic fields, respectively. Based on the amplitude and phase control of the excitation current, the resultant magnetic field generated by the transmitter can always be directed perpendicular to the receiving coil plane, thus forming a targeting magnetic field. To avoid detecting the position and angle of the receiver, a targeting magnetic field control method based on phase difference and duty cycle scanning is proposed. Finally, the efficacy of the proposed methodology is validated through simulation and experimental results.

II. MAGNETIC FIELD ANALYSIS AND CONTROL OF THE MAGNETIC COUPLER

A. *Magnetic Coupler*

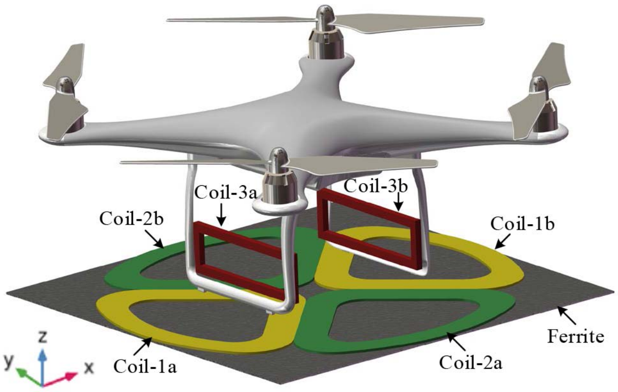

Fig. 1. General overview of the two orthogonal bipolar transmitting coils for UAV-WPT.

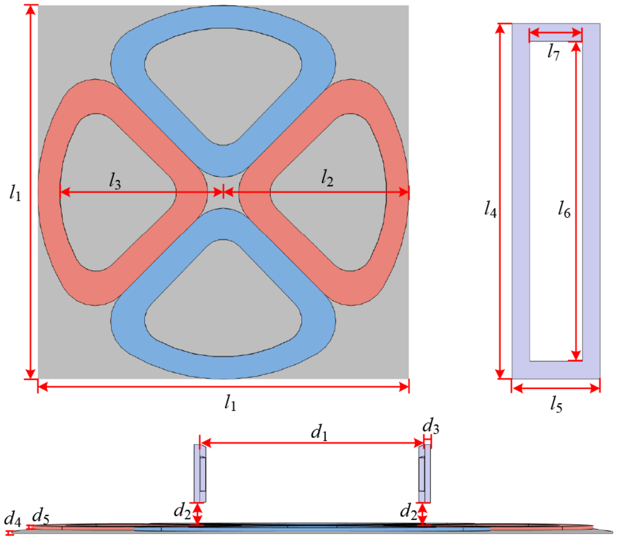

Fig. 2. Dimensional description of the magnetic coupler.

TABLE I
PARAMETERS OF THE MAGNETIC COUPLER

Parameters	Value	Parameters	Value
l_1	500 mm	l_2	250 mm
l_3	190 mm	l_4	200 mm
l_5	50 mm	l_6	180 mm
l_7	30 mm	d_1	200 mm
d_2	20 mm	d_3	5 mm
d_4	2 mm	d_5	3 mm
N_1	10 turns	N_2	10 turns
N_3	10 turns		

Fig. 1 shows the two orthogonal bipolar transmitting coils for UAV-WPT. Coil-1 and Coil-2 are two bipolar coils used as transmitters. Coil-1 comprises Coil-1a and Coil-1b connected in reverse series. Similarly, Coil-2 comprises Coil-2a and Coil-2b connected in reverse series. To reduce magnetic field leakage and enhance coupling, a ferrite is placed at the bottom of the transmitter. Coil-3 is used as a receiver, which consists of two rectangular coils (Coil-3a and Coil-3b) connected in series in the same direction. The receiver is installed on the landing gear of the UAV, which does not change the original appearance of the UAV, nor does it require bulky and fragile ferrite, and has the advantages of easy installation and light weight.

Fig. 2 shows the dimensional description of the proposed magnetic coupler. Based on the dimensions of the Phantom 4-Pro UAV produced by DJI Company, the parameters of the magnetic

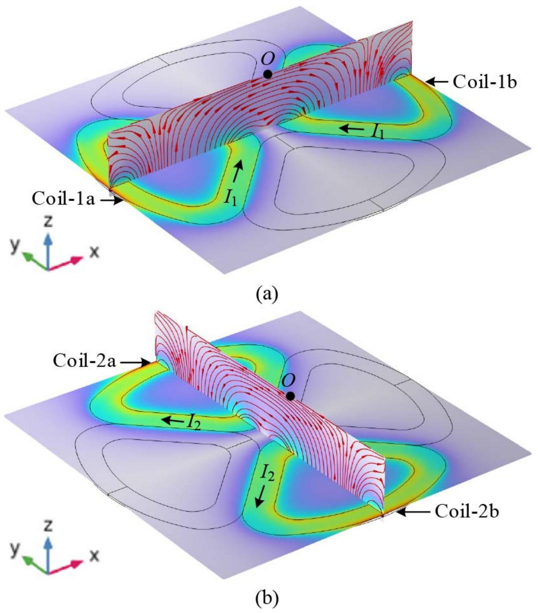

Fig. 3. Magnetic field lines generated by (a) Coil-1 and (b) Coil-2.

coupler are designed as shown in Table I. N_1, N_2, and N_3 are the number of turns of Coil-1, Coil-2, and Coil-3, respectively.

B. Magnetic Field Analysis

Define I_1 and I_2 as the excitation currents for Coil-1 and Coil-2, respectively. When observing the magnetic field distribution generated by Coil-1, set $I_1 = 1$ A and $I_2 = 0$ A. When observing the magnetic field distribution generated by Coil-2, set $I_1 = 0$ A and $I_2 = 1$ A. According to the COMSOL simulation, the magnetic field lines generated by Coil-1 and Coil-2 are calculated as shown in Fig. 3. Coil-1 and Coil-2 generate a magnetic field mainly in the x-direction and y-direction, respectively. According to magnetic field vector superposition principle, the resultant magnetic field generated by two coils is mainly concentrated in the horizontal direction (i.e., x-y plane). The vertically placed rectangular receiving Coil-3 needs to capture the horizontal magnetic field. This indicates that the magnetic fields of the transmitter and receiver are well matched. In addition, compared to traditional circular coils that generate magnetic fields mainly in the vertical direction (i.e., z-direction), the proposed transmitter that generates magnetic fields mainly in the horizontal direction is advantageous in reducing electromagnetic interference to UAV equipment. In addition, Fig. 3 also indicates that the magnetic fields generated by the two transmitting coils are orthogonal. Therefore, the two transmitting coils are mutually decoupled naturally, which is conducive to controlling their excitation currents independently.

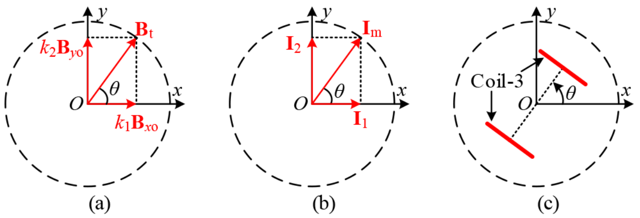

Fig. 4. Control principle of a targeting magnetic field. (a) Resultant magnetic field vector. (b) Resultant current vector. (c) Definition of the receiver's angular misalignment.

C. Control Principle of a Targeting Magnetic Field

A targeting magnetic field refers to the magnetic field generated by the transmitter that is always perpendicular to the receiver, regardless of the position and angle of the receiver. Therefore, controlling the transmitter to generate a targeting magnetic field can improve the magnetic field utilization rate, thereby enhancing the power transfer efficiency. This article takes point O directly above the transmitter as an example to illustrate the control principle of a targeting magnetic field control. As shown in Fig. 3, the magnetic fields generated by Coil-1 and Coil-2 at point O are along the x- and y-directions, respectively. Therefore, it can be assumed that the magnetic fields generated by Coil-1 and Coil-2 at point O under unit excitation current are $\mathbf{B}_{x0}$ and $\mathbf{B}_{y0}$, respectively. Therefore, $\mathbf{B}_{x0}$ and $\mathbf{B}_{y0}$ can be regarded as a set of magnetic field basis vectors. As shown in Fig. 4(a), the resultant magnetic field $\mathbf{B}_\mathrm{t}$ can be linearly represented by $\mathbf{B}_{x0}$ and $\mathbf{B}_{y0}$ as follows:

$$\mathbf{B}_\mathrm{t} = k_1\mathbf{B}_{x0} + k_2\mathbf{B}_{y0}. \tag{1}$$

Define θ as the angle between $\mathbf{B}_\mathrm{t}$ and the positive x-axis direction. $\mathrm{k}_1\mathbf{B}_{x0}$ represents the x-directional magnetic flux density generated by Coil-1 under the excitation current of I_1, $\mathrm{k}_2\mathbf{B}_{y0}$ represents the y-directional magnetic flux density generated by Coil-2 under the excitation current of I_2. According to the Biot–Savart law, k_1 is proportional to I_1, and k_2 is proportional to I_2. Therefore, the resultant magnetic field vector can be directed in any desired direction by controlling I_1 and I_2.

For the receiver to pick up the same power at various angles, it is necessary to make the amplitude of the resultant magnetic field equal in all directions. Therefore, I_1, I_2, and the resultant current vector I_m [see Fig. 4(b)] should satisfy the following relationship:

$$\begin{cases} I_1 = I_\mathrm{m}\cos\theta \\ I_2 = I_\mathrm{m}\sin\theta \end{cases}. \tag{2}$$

This article defines the receiver's angular misalignment as the angle between the line connecting the centers of two rectangular coils and the positive x-axis direction, as shown in Fig. 4(c). To improve power transmission efficiency, it is necessary to make the resultant magnetic field perpendicular to the receiver; that is, the angle of the resultant magnetic field should be the same as the angular misalignment of the receiver. Therefore, θ is also defined as the angular misalignment of the receiver.

According to (2), when the two excitation currents are in a complementary relationship, the resultant current vector modulus remains constant because of $\sqrt{(I_\mathrm{m}\cos\theta)^2 + (I_\mathrm{m}\sin\theta)^2} = I_\mathrm{m}$. Therefore, the modulus of the resultant magnetic field under different θ remains unchanged, which is beneficial for

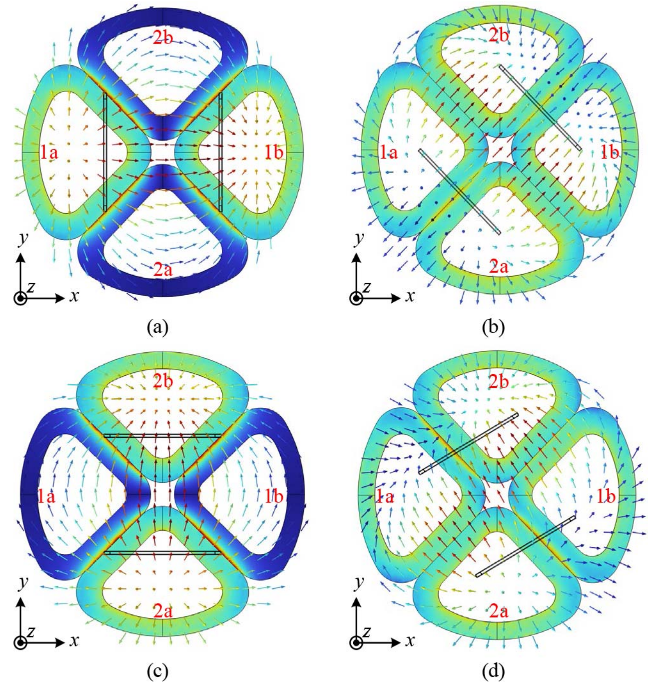

Fig. 5. Relationship between the targeting magnetic field and excitation currents under several angular misalignments of the receiver. (a) $\theta = 0°$, $I_1 = 1$ A, $I_2 = 0$ A. (b) $\theta = 45°$, $I_1 = 0.707$ A, $I_2 = 0.707$ A. (c) $\theta = 90°$, $I_1 = 0$ A, $I_2 = 1$ A. (d) $\theta = 120°$, $I_1 =$ -0.5 A, $I_2 = 0.866$ A.

the receiver to pick up the same power in various angular misalignments.

Fig. 5 shows the relationship between the targeting magnetic field and excitation currents under several angular misalignments of the receiver. For simplicity, let $I_{\mathrm{m}} = 1$ A. When there is no angular misalignment, i.e., $\theta = 0°$. To generate a targeting magnetic field, the excitation currents need to be set to $I_1 = \cos 0° = 1$ A, $I_2 = \sin 0° = 0$ A according to (2), as shown in Fig. 5(a). When the angular misalignment of the receiver θ is 45°, the excitation currents need to be set to $I_1 = \cos 45° = 0.707$ A, $I_2 = \sin 45° = 0.707$ A, as shown in Fig. 5(b). When the angular misalignment of the receiver θ is 90°, the excitation currents need to be set to $I_1 = \cos 90° = 0$ A, $I_2 = \sin 90° = 1$ A, as shown in Fig. 5(c). When the angular misalignment of the receiver θ is 120°, the excitation currents need to be set to $I_1 = \cos 120° =$ -0.5 A, $I_2 = \sin 120° = 0.866$ A, as shown in Fig. 5(d). It is worth noting that if the signs (positive or negative) of I_1 and I_2 are the same, it indicates that the phases of I_1 and I_2 are in the same phase. If the signs of I_1 and I_2 are different, it indicates that the phase of I_1 and I_2 is reversed. Generally, as shown in (2), when the receiver angular misalignment θ is between 0°-90° and 90°-180°, the two excitation currents should be set in the same phase and reverse phase, respectively.

According to the above analysis, to obtain a targeting magnetic field, the amplitude and phase of the excitation currents should vary with the receiver angular misalignment based on the mapping relationship in (2). However, the receiver angular misalignment θ is not known in advance. If we use an attitude sensor to detect the receiver angular misalignment, and then use a communication link to transmit angular misalignment information to the primary-side controller. However, this method is more complex and costly. Since a targeting magnetic field and maximum efficiency transmission are equivalent, the excitation currents can be optimized from the perspective of maximum efficiency transmission to generate a targeting magnetic field. In this method, only the system's dc input current, rather than the receiver's angular misalignment, is required to be detected. Therefore, its implementation is simpler, and specific methods will be provided later.

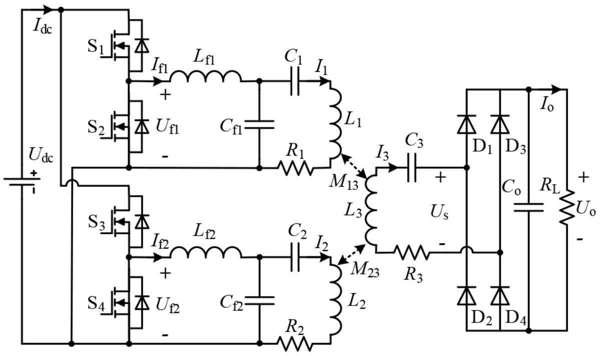

Fig. 6. Circuit topology.

III. System Modeling and Analysis

A. Circuit Topology

The circuit topology of the proposed system is shown in Fig. 6. The self-inductances of Coil-1, Coil-2, and Coil-3 are denoted as L_1, L_2, and L_3, respectively. The mutual inductances between Coil-1 and Coil-3, and between Coil-2 and Coil-3, are represented by M_{13} and M_{23}. Two *LCC* compensation networks, composed of L_{f1}-C_{f1}-C_1 and L_{f2}-C_{f2}-C_2, are adopted on the primary side in this article due to its following advantages: 1) robustness against coupling and load variations; 2) simplified excitation current control; and 3) easy to achieve zero-voltage switching. Two independent half-bridge inverters are employed to drive the two coils separately. The main reason for choosing two half-bridge inverters instead of two full-bridge inverters is that the former requires fewer switches. The Inverter-1 and Inverter-2 are composed of MOSFETS S_1-S_4. On the receiver side, a simplified series-compensated capacitor C_3 combined and a full-bridge rectifier (diodes D_1–D_4) topology are adopted. In Fig. 4, U_{dc} and I_{dc} are the dc input voltage and current of the system, respectively. U_{f1}, U_{f2}, I_{f1}, and I_{f2} are the output voltages and currents of Inverter-1 and Inverter-2. I_1, I_2, and I_3 are the currents flowing through Coil-1, Coil-2, and Coil-3, respectively. R_1, R_2, and R_3 are the equivalent series resistances (ESR) of Coil-1, Coil-2, and Coil-3, respectively. C_{o} is a filtering capacitor. R_{L} is the load resistance. U_{o} and I_{o} represent the system output voltage and current.

B. Excitation Currents Calculation

As analyzed in the previous section, the amplitude and phase of the excitation currents need to change with various positions and angles of the receiver. This article uses pulsewidth modulation (PWM) to control the output voltage of two half-bridge inverters, thereby controlling the excitation currents. To maintain the cos-sin complementary relationship of the excitation currents of (2), the duty cycles of Inverter-1 and Inverter-2 can be set to 0.5-α and α, respectively, where $0\leq\alpha\leq0.5$. Because *LCC* compensation networks can effectively filter out high-order harmonics generated by inverters and rectifiers, the fundamental harmonic approximation (FHA) method is used for modeling. Hence, $\mathbf{U}_{\mathrm{f1}}$ and $\mathbf{U}_{\mathrm{f2}}$ can be expressed as follows:

$$\begin{cases}\mathbf{U}_{\mathrm{f1}} = \frac{\sqrt{2}U_{\mathrm{dc}}}{\pi}\sin\left((0.5-\alpha)\pi\right) = \cos(\alpha\pi)\,e^{\mathrm{j}\beta} \\ \mathbf{U}_{\mathrm{f2}} = \frac{\sqrt{2}U_{\mathrm{dc}}}{\pi}\sin(\alpha\pi)\end{cases}, \beta = 0 \text{ or } \pi \tag{3}$$

where β is the phase difference between $\mathbf{U}_{\mathrm{f1}}$ and $\mathbf{U}_{\mathrm{f2}}$. $\beta = 0$ indicates that $\mathbf{U}_{\mathrm{f1}}$ and $\mathbf{U}_{\mathrm{f2}}$ are in the same phase; $\beta = \pi$ indicates that $\mathbf{U}_{\mathrm{f1}}$ and $\mathbf{U}_{\mathrm{f2}}$ are in reverse phase.

The resonance relationship of the system can be expressed as follows:

$$\begin{aligned}\omega = 2\pi f &= \frac{1}{\sqrt{L_{\mathrm{f1}}C_{\mathrm{f1}}}} = \frac{1}{\sqrt{L_{\mathrm{f2}}C_{\mathrm{f2}}}} = \frac{1}{\sqrt{L_3C_3}} \\ &= \frac{1}{\sqrt{(L_1-L_{\mathrm{f1}})\,C_1}} = \frac{1}{\sqrt{(L_2-L_{\mathrm{f2}})\,C_2}}\end{aligned} \tag{4}$$

where *f* is the operating frequency of the system, and ω is the angular frequency.

For the L_{f1}-C_{f1} and L_{f2}-C_{f2} circuits in Fig. 6, their Kirchhoff Voltage Law (KVL) equations can be expressed as follows:

$$\begin{cases}\mathbf{U}_{\mathrm{f1}} = \mathrm{j}\omega L_{\mathrm{f1}}\mathbf{I}_{\mathrm{f1}} + \frac{1}{\mathrm{j}\omega C_{\mathrm{f1}}}\left(\mathbf{I}_{\mathrm{f1}} - \mathbf{I}_1\right) \\ \mathbf{U}_{\mathrm{f2}} = \mathrm{j}\omega L_{\mathrm{f2}}\mathbf{I}_{\mathrm{f2}} + \frac{1}{\mathrm{j}\omega C_{\mathrm{f2}}}\left(\mathbf{I}_{\mathrm{f2}} - \mathbf{I}_2\right)\end{cases}. \tag{5}$$

The designed parameters of the two transmitting coils and two *LCC* compensation networks are the same. Therefore, to simplify the analysis, it can be assumed that $L_{\mathrm{f}} = L_{\mathrm{f1}} = L_{\mathrm{f2}}$, $C_{\mathrm{f}} = C_{\mathrm{f1}} = C_{\mathrm{f2}}$, $L_{\mathrm{p}} = L_1 = L_2$, $C_{\mathrm{p}} = C_1 = C_2$, and $R_{\mathrm{p}} = R_1 = R_2$. According to (3)–(5), $\mathbf{I}_1$ and $\mathbf{I}_2$ can be calculated as follows:

$$\begin{cases}\mathbf{I}_1 = \frac{\sqrt{2}U_{\mathrm{dc}}}{\mathrm{j}\pi\omega L_{\mathrm{f}}}\cos(\alpha\pi)\,e^{\mathrm{j}\beta} \\ \mathbf{I}_2 = \frac{\sqrt{2}U_{\mathrm{dc}}}{\mathrm{j}\pi\omega L_{\mathrm{f}}}\sin(\alpha\pi)\end{cases}, \beta = 0 \text{ or } \pi. \tag{6}$$

In (6), the parameters U_{dc}, ω, and L_{f} will not change when the system is in operation. Hence, the amplitudes of $\mathbf{I}_1$ and $\mathbf{I}_2$ are only related to the duty cycle α. $\mathbf{I}_1$ and $\mathbf{I}_2$ can be kept in the same phase or reverse phase by controlling β. Therefore, we can optimize α and β to achieve a targeting magnetic field. It is worth mentioning that if two full-bridge inverters are employed on the transmitter side, the amplitude and phase of the two excitation currents can be adjusted by controlling the phase-shift angles and phase differences of the two full-bridge inverters, thereby generating a targeting magnetic field.

Fig. 7 shows the example waveforms of the inverter output voltages and excitation currents, which further illustrate the effects of α and β on the amplitude and phase of the excitation currents. U_{ref} is a square wave with a frequency of *f*, a period of *T*, and a duty cycle of 0.5. U_{ref} is only used to represent the temporal relationship of other waveforms and has no practical significance. As shown in Fig. 7(a), when the Inverter-2's duty cycle α is set to 0.2, according to the complementary relationship, the Inverter-1's duty cycle needs to be set to 0.3, and the amplitude of I_1 is greater than that of I_2. When β is set to 0, it is necessary to adjust the timing of the driving signals of Inverter-1 and Inverter-2 to keep U_{f1} and U_{f2} in the same phase, thereby keeping I_1 and I_2 in the same phase. As shown in Fig. 7(b), when the Inverter-2's duty cycle α is set to 0.3, according to the complementary relationship, the Inverter-1's duty cycle needs to be set to 0.2, and the amplitude of I_1 is smaller than that of I_2. When β is set to π, it is necessary to adjust the timing of the driving signals of Inverter-1 and Inverter-2 to keep U_{f1} and U_{f2} in reverse phase, thereby keeping I_1 and I_2 in reverse phase. It is worth mentioning that the excitation current in Fig. 7 lags behind the corresponding inverter's output voltage by 90°, and its lag can be explained by (6).

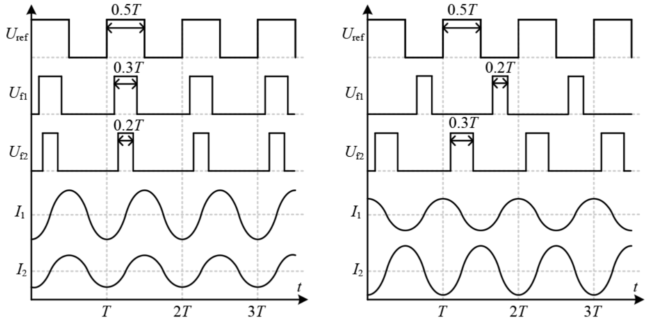

(a) (b)

Fig. 7. Example waveforms of the inverter output voltages and excitation currents when (a) $\alpha = 0.2$, $\beta = 0$ and (b) $\alpha = 0.3$, $\beta = \pi$.

C. Analysis of Maximum Output Power Transmission Conditions

The secondary-side KVL equation based on the mutual coupling theory can be expressed as follows:

$$j\omega M_{13}\boldsymbol{I}_1 + j\omega M_{23}\boldsymbol{I}_2 = \left(j\omega L_3 + \frac{1}{j\omega C_3} + R_3 + R_{\mathrm{eq}}\right)\boldsymbol{I}_3 \tag{7}$$

where R_{eq} is the equivalent load before full-bridge rectifier, which can be expressed as follows:

$$R_{\mathrm{eq}} = \frac{8R_{\mathrm{L}}}{\pi^2}. \tag{8}$$

According to (4), (6), (7), and (8), $\mathbf{I}_3$ can be calculated as follows:

$$\mathbf{I}_3 = \frac{\sqrt{2}U_{\mathrm{dc}}\left(M_{13}\cos(\alpha\pi)\,e^{\mathrm{j}\beta} + M_{23}\sin(\alpha\pi)\right)}{\pi L_{\mathrm{f}}\left(R_3 + 8R_{\mathrm{L}}/\pi^2\right)}. \tag{9}$$

According to the characteristics of the full-bridge rectifier, the system output voltage U_{o} can be expressed as follows:

$$\begin{aligned}U_{\mathrm{o}} = I_{\mathrm{o}}R_{\mathrm{L}} &= \frac{2\sqrt{2}}{\pi}\left|\mathbf{I}_3\right|R_{\mathrm{L}} \\ &= \frac{4U_{\mathrm{dc}}R_{\mathrm{L}}\left|M_{13}\cos(\alpha\pi)\,e^{\mathrm{j}\beta} + M_{23}\sin(\alpha\pi)\right|}{\pi^2L_{\mathrm{f}}\left(R_3 + 8R_{\mathrm{L}}/\pi^2\right)}.\end{aligned} \tag{10}$$

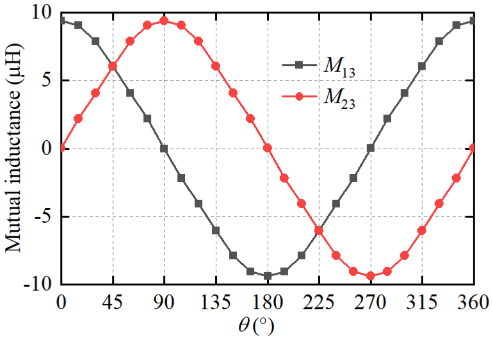

Fig. 8. Simulated mutual inductance varies with the receiver's angular misalignment.

The system output power P_o can be expressed as follows:

$$P_\mathrm{o} = \frac{U_\mathrm{o}^2}{R_\mathrm{L}} = \frac{16U_\mathrm{dc}^2\left(M_{13}\cos\left(\alpha\pi\right)\mathrm{e}^{\mathrm{j}\beta} + M_{23}\sin\left(\alpha\pi\right)\right)^2 R_\mathrm{L}}{\pi^4 L_\mathrm{f}^2\left(R_3 + 8R_\mathrm{L}/\pi^2\right)^2}. \tag{11}$$

From (11), after the circuit parameters of the system are determined, the output power is determined by M_{13}, M_{23}, α, and β. According to the COMSOL simulation calculation, the relationship between mutual inductance and the receiver's angular misalignment is shown in Fig. 8. M_{13} and M_{23} change according to the cosine and sine laws, respectively. When the receiver's angular misalignment is in the angle range of (0°, 90°) and (180°, 270°), the signs of M_{13} and M_{23} are the same, that is, $M_{13}\times M_{23}>0$. When the receiver's angular misalignment is in the angle range of (90°, 180°) and (270°, 360°), the signs of M_{13} and M_{23} are different, that is, $M_{13}\times M_{23}<0$. To avoid the cancellation of picked-up power, β needs to be optimized according to the signs of M_{13} and M_{23}. Specifically, when $M_{13}\times M_{23}>0$, β needs to be set to 0. When $M_{13}\times M_{23}<0$, β needs to be set to π.

After β is determined, (11) can be written in the following form:

$$P_\mathrm{o} = \frac{16U_\mathrm{dc}^2\left(M_{13}^2 + M_{23}^2\right)\sin^2\left(\alpha\pi + \varphi\right)R_\mathrm{L}}{\pi^4 L_\mathrm{f}^2\left(R_3 + 8R_\mathrm{L}/\pi^2\right)^2} \tag{12}$$

where

$$\varphi = \arctan\left|\frac{M_{13}}{M_{23}}\right|, \varphi \in \left(0, \frac{\pi}{2}\right). \tag{13}$$

According to (12), P_o reaches its maximum value when $\sin^2(\alpha\pi + \varphi) = 1$, i.e., $\alpha\pi + \varphi = \frac{\pi}{2}$. Hence, the condition for maximum output power transmission of the system is as follows:

$$\begin{cases} \alpha = \frac{1}{2} - \frac{1}{\pi}\arctan\left|\frac{M_{13}}{M_{23}}\right| \\ \beta = \begin{cases} 0, \text{when} M_{13}\times M_{23} \geq 0 \\ \pi, \text{when} M_{13}\times M_{23} < 0 \end{cases} \end{cases}. \tag{14}$$

TABLE II

ELECTRICAL PARAMETERS IN EXPERIMENT

Parameter	Value	Parameter	Value
U_dc	150 V	f	100 kHz
R_L	10 Ω	L_f1, L_f2	14.9, 15.0 μH
C_f1, C_f2	169.5, 169.7 nF	C_1, C_2, C_3	18.0, 18.1, 35.2 nF
L_1, L_2, L_3	158.2, 158.9, 72.1 μH	R_1, R_2, R_3	0.19, 0.19, 0.08 Ω

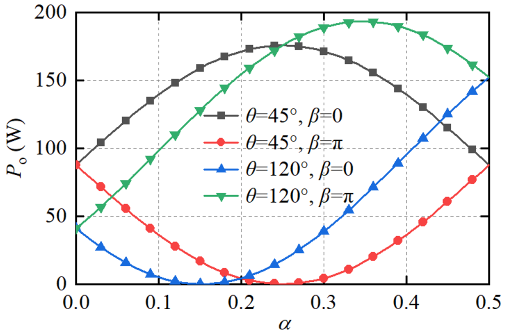

Fig. 9. Calculated output power P_o varies with the duty circle α.

This article selects two types of the receiver's angular misalignments (θ = 45° and 120°) as examples to further explain the conditions for maximum output power transmission. When $\theta = 45°$, according to Fig. 8, $M_{13} = M_{23} = 6$ μH. By substituting these mutual inductance data into (14), the maximum output power condition is that $\alpha = 0.25$ and $\beta = 0$. When $\theta = 120°$, according to Fig. 8, M_{13} = -4.1 μH, M_{23} = 7.9 μH. By substituting these mutual inductance data into (14), the maximum output power condition is that $\alpha = 0.35$ and $\beta = \pi$. To further illustrate that optimizing the duty cycle α and phase difference β can achieve the maximum output power transmission, the relationship between output power and duty cycle is calculated by (11) and the parameters in Table II, as shown in Fig. 9.

When $\theta = 45°$, the maximum output power transmission condition is that $\alpha = 0.25$ and $\beta = 0$. When $\theta = 120°$, the maximum output power transmission condition is that $\alpha = 0.35$ and $\beta = \pi$. The values of α and β corresponding to the maximum output power transmission are consistent with the theoretical calculation of (14). Therefore, Fig. 9 further demonstrates the correctness of (14).

D. Analysis of Maximum Efficiency Transmission Conditions

The KVL equations for the circuit C_f1-C_1-L_1-R_1 and C_f2-C_2-L_2-R_2 based on the mutual coupling theory can be expressed as follows:

$$\begin{cases} \frac{1}{\mathrm{j}\omega C_\mathrm{f1}}\left(\mathbf{I}_\mathrm{f1} - \mathbf{I}_1\right) = \left(\mathrm{j}\omega L_1 + \frac{1}{\mathrm{j}\omega C_1} + R_1\right)\mathbf{I}_1 - \mathrm{j}\omega M_{13}\mathbf{I}_3 \\ \frac{1}{\mathrm{j}\omega C_\mathrm{f2}}\left(\mathbf{I}_\mathrm{f2} - \mathbf{I}_2\right) = \left(\mathrm{j}\omega L_2 + \frac{1}{\mathrm{j}\omega C_2} + R_2\right)\mathbf{I}_1 - \mathrm{j}\omega M_{23}\mathbf{I}_3 \end{cases}. \tag{15}$$

According to (2), (4), and (9), $\mathbf{I}_\mathrm{f1}$ and $\mathbf{I}_\mathrm{f2}$ can be calculated as follows:

$$\begin{cases} \boldsymbol{I}_\mathrm{f1} = \frac{\sqrt{2}U_\mathrm{dc}M_{13}\left(M_{13}\cos(\alpha\pi)e^{j\beta} + M_{23}\sin(\alpha\pi)\right)}{\pi L_f^2\left(R_3 + \frac{8R_L}{\pi^2}\right)} \\ \qquad + \frac{\sqrt{2}U_\mathrm{dc}R_1\cos(\alpha\pi)e^{j\beta}}{\pi\omega^2 L_f^2} \\ \boldsymbol{I}_\mathrm{f2} = \frac{\sqrt{2}U_\mathrm{dc}M_{23}\left(M_{13}\cos(\alpha\pi)e^{j\beta} + M_{23}\sin(\alpha\pi)\right)}{\pi L_f^2\left(R_3 + \frac{8R_L}{\pi^2}\right)} \\ \qquad + \frac{\sqrt{2}U_\mathrm{dc}R_2\sin(\alpha\pi)}{\pi\omega^2 L_f^2}. \end{cases} \tag{16}$$

Since (16) has no imaginary part, each inverter's output voltage and current are in the same phase. If the losses of the two inverters are ignored, the output power of the two inverters is equal to the input power, which can be expressed as follows:

$$U_{\mathrm{dc}} I_{\mathrm{dc}} = \left|\mathbf{U}_{\mathrm{f1}} \mathbf{I}_{\mathrm{f1}}\right| + \left|\mathbf{U}_{\mathrm{f2}} \mathbf{I}_{\mathrm{f2}}\right|. \tag{17}$$

By substituting (3) into (17), the system's dc input current I_{dc} can be expressed as follows:

$$I_{\mathrm{dc}} = \frac{\sqrt{2}}{\pi} \cos(\alpha\pi)\, e^{\mathrm{j}\beta} \left|\mathbf{I}_{\mathrm{f1}}\right| + \frac{\sqrt{2}}{\pi} \sin(\alpha\pi) \left|\mathbf{I}_{\mathrm{f2}}\right|. \tag{18}$$

By substituting (16) into (18) and simplifying it, I_{dc} can be expressed as follows:

$$\begin{aligned} I_{\mathrm{dc}} &= \frac{2U_{\mathrm{dc}}\left(M_{13}\cos(\alpha\pi)\, e^{\mathrm{j}\beta} + M_{23}\sin(\alpha\pi)\right)^2}{\pi^2 L_{\mathrm{f}}^2 \left(R_3 + 8R_{\mathrm{L}}/\pi^2\right)} + \frac{2U_{\mathrm{dc}} R_{\mathrm{p}}}{\pi^2 \omega^2 L_{\mathrm{f}}^2} \\ &= \frac{2U_{\mathrm{dc}}\left(M_{13}^2 + M_{23}^2\right)\sin^2(\alpha\pi + \varphi)}{\pi^2 L_{\mathrm{f}}^2 \left(R_3 + 8R_{\mathrm{L}}/\pi^2\right)} + \frac{2U_{\mathrm{dc}} R_{\mathrm{p}}}{\pi^2 \omega^2 L_{\mathrm{f}}^2}. \end{aligned} \tag{19}$$

The system input power P_{in} can be expressed as follows:

$$\begin{aligned} P_{\mathrm{in}} &= \frac{2U_{\mathrm{dc}}^2\left(M_{13}\cos(\alpha\pi)\, e^{\mathrm{j}\beta} + M_{23}\sin(\alpha\pi)\right)^2}{\pi^2 L_{\mathrm{f}}^2 \left(R_3 + 8R_{\mathrm{L}}/\pi^2\right)} + \frac{2U_{\mathrm{dc}}^2 R_{\mathrm{p}}}{\pi^2 \omega^2 L_{\mathrm{f}}^2} \\ &= \frac{2U_{\mathrm{dc}}^2\left(M_{13}^2 + M_{23}^2\right)\sin^2(\alpha\pi + \varphi)}{\pi^2 L_{\mathrm{f}}^2 \left(R_3 + 8R_{\mathrm{L}}/\pi^2\right)} + \frac{2U_{\mathrm{dc}}^2 R_{\mathrm{p}}}{\pi^2 \omega^2 L_{\mathrm{f}}^2}. \end{aligned} \tag{20}$$

According to (19) and (20), both I_{dc} and P_{in} reach their maximum values when $\sin^2(\alpha\pi + \varphi) = 1$, i.e., $\alpha\pi + \varphi = \frac{\pi}{2}$. Hence, the conditions for maximum input current and input power of the system are also given by (14).

The system efficiency η can be expressed as follows:

$$\eta = \frac{8R_{\mathrm{L}}/\pi^2}{\frac{\left(R_3 + \left(8R_{\mathrm{L}}/\pi^2\right)\right)^2 R_{\mathrm{p}}}{\omega^2\left(M_{13}^2 + M_{23}^2\right)\sin^2(\alpha\pi + \varphi)} + R_3 + \left(8R_{\mathrm{L}}/\pi^2\right)}. \tag{21}$$

According to (21), η reaches its maximum value when $\sin^2(\alpha\pi + \varphi) = 1$, i.e., $\alpha\pi + \varphi = \frac{\pi}{2}$. Hence, the condition for maximum efficiency transmission of the system is also given by (14). It is worth noting that for the convenience of theoretical derivation, this article ignores the losses of the inverters, compensation networks, and rectifier. Therefore, the efficiency of (21) essentially refers to the magnetic coupler's efficiency. The maximum efficiency transmission mentioned in the theoretical analysis section of this article refers to the efficiency of the magnetic coupler, while the efficiency in the experimental section refers to the dc-to-dc efficiency.

The relationship between system efficiency and duty cycle is calculated based on (21) and the parameters in Table II, as shown in Fig. 10. When $\theta = 45°$, the maximum efficiency transmission condition is that $\alpha = 0.25$ and $\beta = 0$. When $\theta = 120°$, the maximum efficiency transmission condition is that $\alpha = 0.35$ and $\beta = \pi$. Figs. 9 and 10 further illustrate that the conditions for achieving maximum output power transmission and maximum efficiency transmission are the same, i.e, α and β satisfy (14).

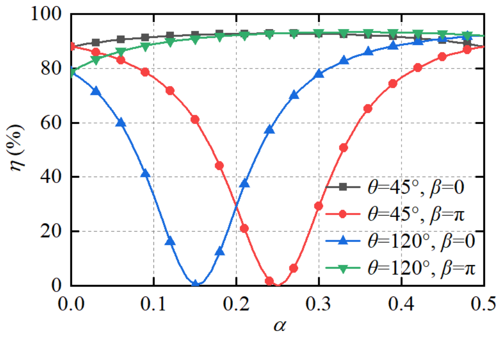

Fig. 10. Calculated system efficiency η varies with the duty circle α.

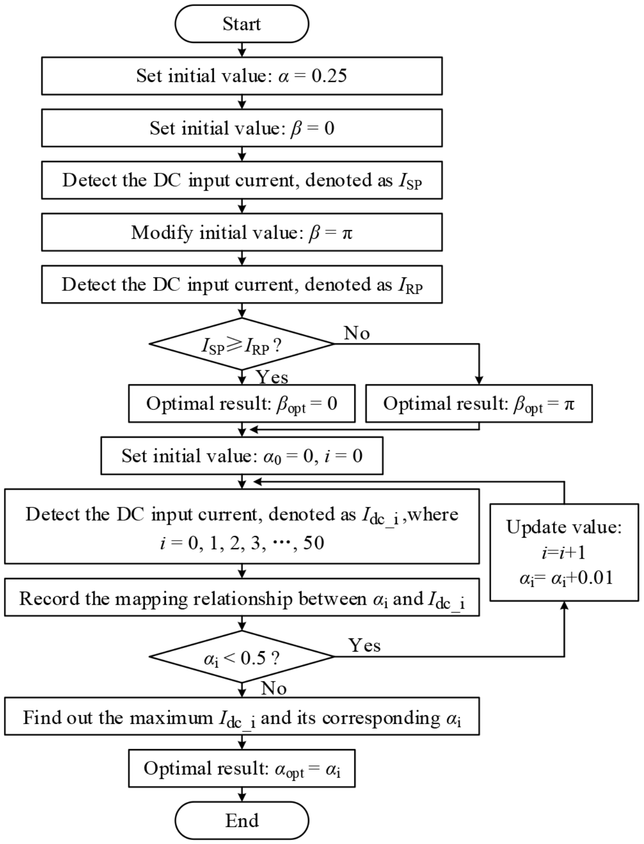

Fig. 11. Flowchart of the targeting magnetic field control method based on phase difference and duty cycle scanning.

IV. TARGETING MAGNETIC FIELD CONTROL METHOD

A. Flowchart of the Targeting Magnetic Field Control Method

This article will generate a targeting magnetic field from the perspective of achieving maximum efficiency transmission. According to (19) and (21), the conditions for achieving maximum efficiency transmission and achieving maximum input current are the same, i.e, α and β satisfy (14). Therefore, based on phase difference and duty cycle scanning and input current detection, the maximum efficiency point can be found to achieve a targeting magnetic field. Fig. 11 shows the flowchart of the targeting magnetic field control method.

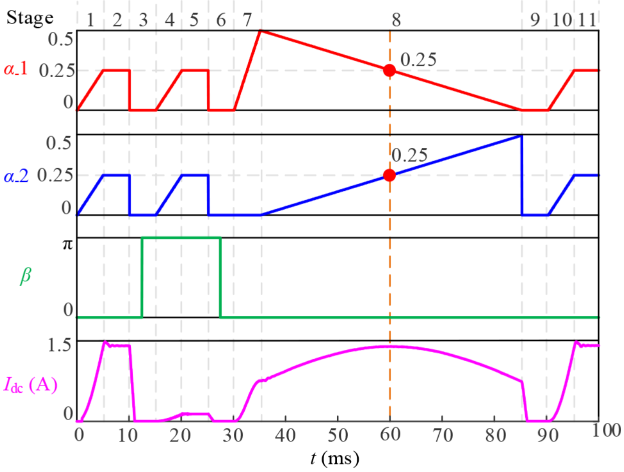

Fig. 12. Simulated waveforms of α, β, and I_{dc} when $\theta = 45°$.

First, it is necessary to determine the phase difference between the two excitation currents, that is, whether the value of β is 0 or π. The specific method is as follows: First, set the duty cycle of both inverters to 0.25. Then, let the two inverters operate in the same phase and reverse phase states, respectively. Subsequently, the dc input currents in the same phase and reverse phase operating states are detected separately, denoted as I_{SP} and I_{RP}, respectively. Then, compare the sizes of I_{SP} and I_{RP}. If I_{SP} is greater than or equal to I_{RP}, the optimized value β_{opt} is 0; otherwise, the optimized value β_{opt} is π.

After the phase difference is optimized, the next step requires optimizing the amplitude relationship between the two excitation currents, that is, optimizing the duty cycle of the two inverters, 0.5-α and α. We use the duty cycle scanning method to find the optimal duty cycle α_{opt}. The specific method is as follows: First, increase the value of the duty cycle α_{i} ($i = 0, 1, 2, \ldots, 50$) from 0 to 0.5 in steps of 0.01. Subsequently, detect and record the dc input current $I_{\mathrm{dc\_i}}$ corresponding to each duty cycle α_{i}. Next, find the maximum value of ($I_{\mathrm{dc\_1}}, I_{\mathrm{dc\_2}}, \ldots, I_{\mathrm{dc\_50}}$) and its corresponding α_{i}. This α_{i} is the optimal duty cycle α_{opt}. Finally, let Inverter-1 and Inverter-2 operate in the states of duty cycle 1-α_{opt} and α_{opt}, respectively, with a phase difference of β_{opt}. The excitation currents generated by this optimized state can cause the transmitter to generate a targeting magnetic field. This conclusion will be proven in detail in Fig. 16.

B. Typical Applications of Phase Difference and Duty Cycle Scanning

To further illustrate the specific implementation process of the targeting magnetic field control method based on phase difference and duty cycle scanning, this article selects two types of the receiver's angular misalignment ($\theta = 45°$ and $120°$) as examples to explain. According to Fig. 8, when $\theta = 45°$, $M_{13} = M_{23} = 6\ \mu$H. Based on the parameters in Table II and MATLAB/Simulink simulation, the waveforms of the duty cycle α, phase difference β, and input current I_{dc} are calculated as shown in Fig. 12, where α_1 and α_2 represent the duty cycles of Inverter-1 and Inverter-2, respectively. $\alpha\_1 = 0.5$-α, $\alpha\_2 = \alpha$. The specific process of the targeting magnetic field control method can be divided into 11 stages.

Stage 1–6 uses phase difference scanning method to find the optimal phase difference β_{opt}. To avoid significant overshoot of input current during the start-up process, soft start is adopted in stage 1. Specifically, slowly increase the duty cycle of the two inverters from 0 to 0.25, with a soft start duration of 5 ms. In stage 2, let the two inverters operate in the same phase state ($\beta = 0$) for 5 ms, during which the input current is detected and denoted as I_{SP}. To avoid a significant overshoot of input current caused by switching directly from the same phase state to reverse phase state, the two inverters are kept in the OFF state for 5 ms in stage 3 to release power. Then, perform a soft start in stage 4 with a duration of 5 ms. In stage 5, let the two inverters operate in reverse phase state ($\beta = \pi$) for 5 ms, during which the input current is detected and denoted as I_{RP}. In stage 6, keep both inverters turned OFF for 5 ms to release power. From Fig. 12, it can be seen that $I_{\mathrm{SP}} = 1.31$ A, $I_{\mathrm{RP}} = 0.13$ A, and $I_{\mathrm{SP}} > I_{\mathrm{RP}}$. Therefore, the optimal value of β_{opt} is 0, which means that both inverters will operate in the same phase in the subsequent stages. According to (14), when $M_{13} \times M_{23} > 0$, the value of β should be designed as 0. Therefore, the scanning result of the phase difference is consistent with (14).

Stage 7–9 uses duty cycle scanning method to find the optimal duty cycle α_{opt}. In stage 7, Inverter-1 operates with a soft start for 5 ms, while Inverter-2 remains in the OFF state. In stage 8, let α increase from 0 to 0.5 with a step size of 0.01, and change the duty cycle every 1 ms for a total of 50 times, with a duration of 50 ms. At the same time, record the input current corresponding to each duty cycle. Then, turn OFF two inverters in stage 9 for 5 ms and find the optimal α corresponding to the maximum input current. From Fig. 12, it can be seen that the maximum input current is 1.31 A, corresponding to α_{opt} of 0.25. When $M_{13} = M_{23} = 6\ \mu$H, according to (15), the value of α can be calculated as 0.25. Therefore, the scanning result of the duty cycle is consistent with (14).

In stage 10, soft start is adopted with a duration of 5 ms. In stage 11, let both inverters operate at the optimized phase difference and duty cycle state ($\beta_{\mathrm{opt}} = 0$, $\alpha_{\mathrm{opt}} = 0.25$). As shown in Fig. 12, through phase difference and duty cycle scanning, as well as input current detection, it only takes 85 ms to find the optimal values of α and β. Fig. 13 shows the simulated waveforms of two inverters' output voltages (U_{f1} and U_{f2}) and excitation currents (I_1 and I_2) when $\theta = 45°$. In Fig. 13, two enlarged views represent the waveforms at the same phase stage and the reverse phase stage, respectively.

Fig. 14 shows the simulated waveforms of α, β, and I_{dc} when $\theta = 120°$, where $M_{13} = -4.1\ \mu$H and $M_{23} = 7.9\ \mu$H (see Fig. 8). The processes in Figs. 14 and 12 are the same, except that the input current values detected at certain stages are different, resulting in different optimization values for α_{opt} and β_{opt}. In the phase difference scanning stage, the input currents in the same phase and reverse phase states are $I_{\mathrm{SP}} = 0.22$ A (see stage 2) and $I_{\mathrm{RP}} = 1.32$ A (see stage 5), respectively. Since $I_{\mathrm{SP}} < I_{\mathrm{RP}}$, the optimized value of β_{opt} is π. During the duty cycle scanning stage, the detected maximum input current is 1.35 A (see stage

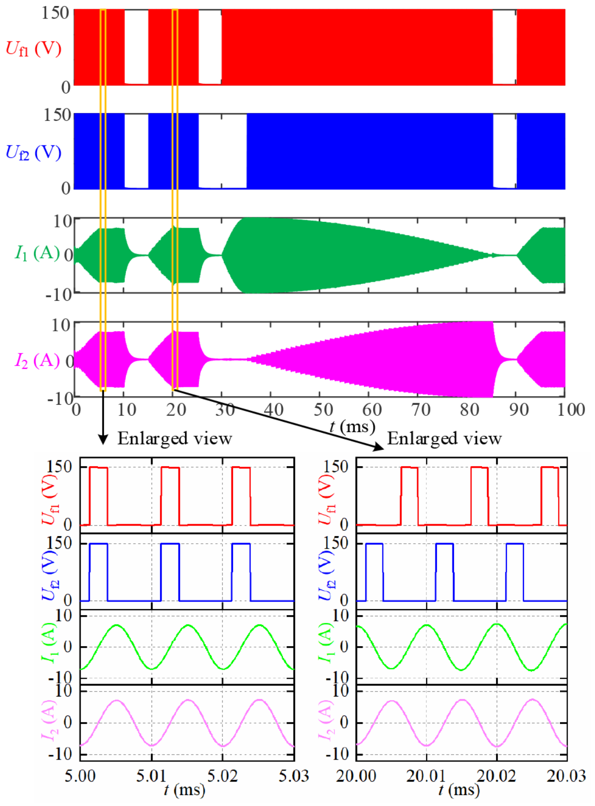

Fig. 13. Simulated waveforms of $U_{\rm f1}$, $U_{\rm f2}$, I_1, and I_2 when $\theta = 45°$.

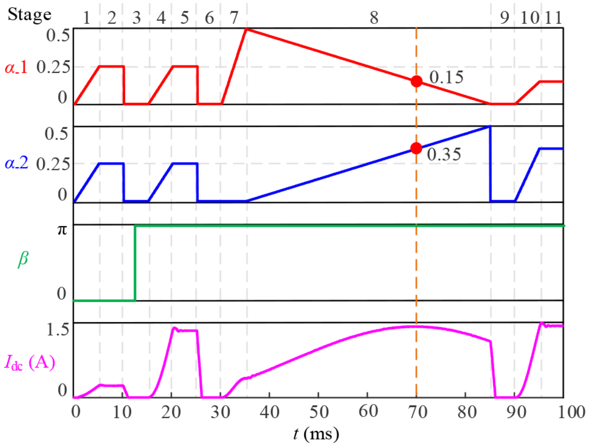

Fig. 14. Simulated waveforms of α, β, and $I_{\rm dc}$ when $\theta = 120°$.

2), corresponding to an optimized value of 0.35 for $\alpha_{\rm opt}$. Finally, let the two inverters operate with duty cycles of 0.15 and 0.35, respectively, and maintain the reverse phase state (see stage 11). According to (14), when $M_{13} = $ -4.1 μH and $M_{23} = 7.9$ μH, the value of α and β can be calculated as 0.35 and π, respectively. Therefore, the scanning result of the phase difference and duty cycle is consistent with (14).

Fig. 15 shows the simulated waveforms of two inverters' output voltages ($U_{\rm f1}$ and $U_{\rm f2}$) and excitation currents (I_1 and I_2) when $\theta = 120°$. In Fig. 15, two enlarged views represent the waveforms at the duty cycle scanning stage and final optimized operational state, respectively.

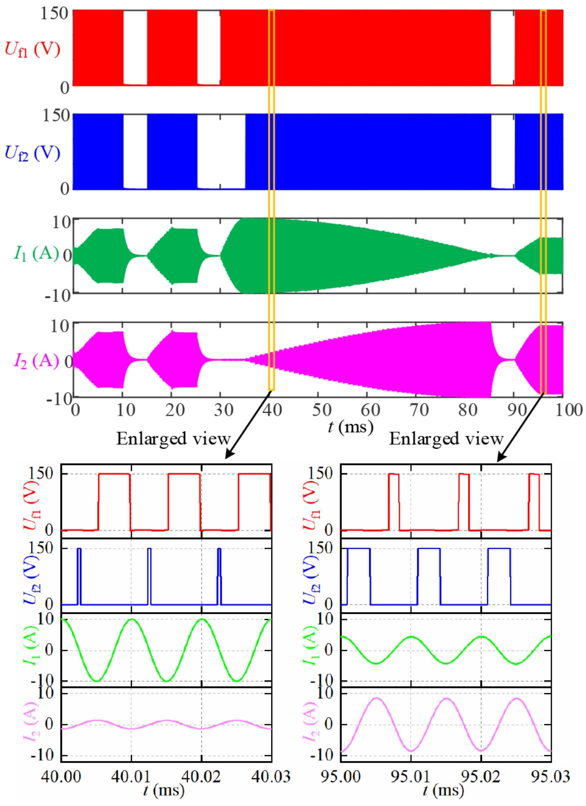

Fig. 15. Simulated waveforms of $U_{\rm f1}$, $U_{\rm f2}$, I_1, and I_2 when $\theta = 120°$.

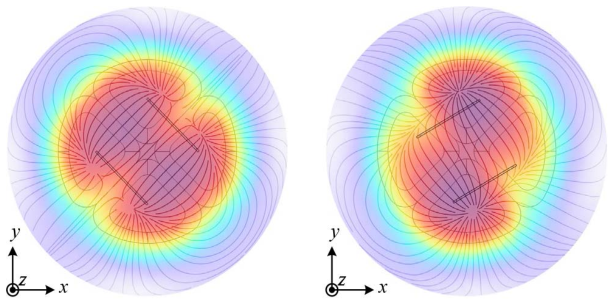

(a) (b)

Fig. 16. Magnetic field distribution generated by the transmitter under the optimized excitation currents. (a) $\theta = 45°$, $I_1 = I_2 = 5.1$ A. (b) $\theta = 120°$, $I_1 =$ -3.31 A, $I_2 = 6.38$ A.

Fig. 16 shows the magnetic field distribution generated by the transmitter under optimized excitation current. When the receiver's angular misalignment θ is 45°, from Fig. 12, the optimized values of $\alpha_{\rm opt}$ and $\beta_{\rm opt}$ are 0.25 and 0, respectively. When two inverters are operating in the final optimized state, the simulation calculation shows that the root mean square (RMS) values of the excitation currents I_1 and I_2 are both 5.1 A, and the two excitation currents remain in the same phase. By inputting these two optimized excitation currents into the COMSOL simulation, the magnetic field distribution generated by the transmitter is shown in Fig. 16(a).

When the receiver's angular misalignment θ is 120°, from Fig. 14, the optimized values of $\alpha_{\rm opt}$ and $\beta_{\rm opt}$ are 0.35 and π, respectively. The optimized excitation currents of I_1 and I_2 are

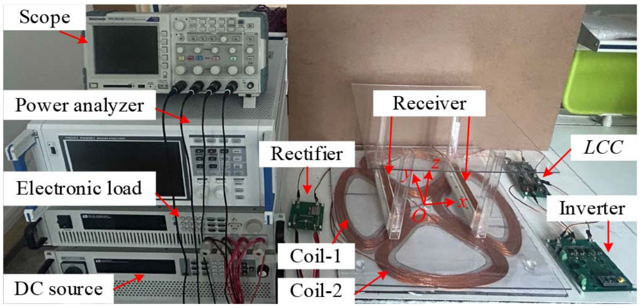

Fig. 17. Experimental prototype.

3.31 A and 6.38 A, respectively, and the two excitation currents remain in the reverse phase. Fig. 16(b) shows the magnetic field distribution generated by the transmitter under the optimized excitation currents when $\theta = 120°$. In Fig. 16, the magnetic field lines generated by the transmitter pass vertically through the receiver. The simulation results in Fig. 16 demonstrate the correctness of optimizing the excitation current through phase difference and duty cycle scanning methods to generate a targeting magnetic field.

V. Experiment Verification

A. Experimental Setup

Fig. 17 shows the experimental prototype of the proposed UAV wireless charging system, where the magnetic coupler parameters are shown in Table I, and the electrical parameters are shown in Table II. An ITECH IT6012D-800-50 and an ITECH IT8514B are used as the dc power supply and electronic load, respectively. Voltages and currents are measured using a Tektronix TPS2014B oscilloscope. Power losses and efficiency are measured with a HIOKI PW6001 power analyzer. Inductance and capacitance are measured using a HIOKI IM3536 LCR meter. Two half-bridge inverters, dc detection circuits, and the control board are integrated onto a single PCB. The MOSFETS used are Infineon IPB60R125C6, and the dc input current is detected using ALLEGRO ACS724LLCTR-05AB-T current sensor chips. The controller is implemented with an STM32F103C8T6 microcontroller. The two *LCC* compensation networks are integrated on another PCB using Bourns PQ2614BLA-150K inductors and TDK CGA6L4C0G2J153G160AA multilayer ceramic capacitor arrays as compensation capacitors. On the receiver side, the series compensation capacitor and full-bridge rectification filter circuit are integrated on a separate PCB using AnBon SU10100-T rectifier diodes. Both the transmitter and the receiver are manufactured using Litz wire with 0.05 mm × 1300 strands. A large shielding core measuring 500 × 500 × 2 mm is formed by arranging 25 PC95-type ferrite cores, each with dimensions of 100 × 100 × 2 mm, beneath the transmitter.

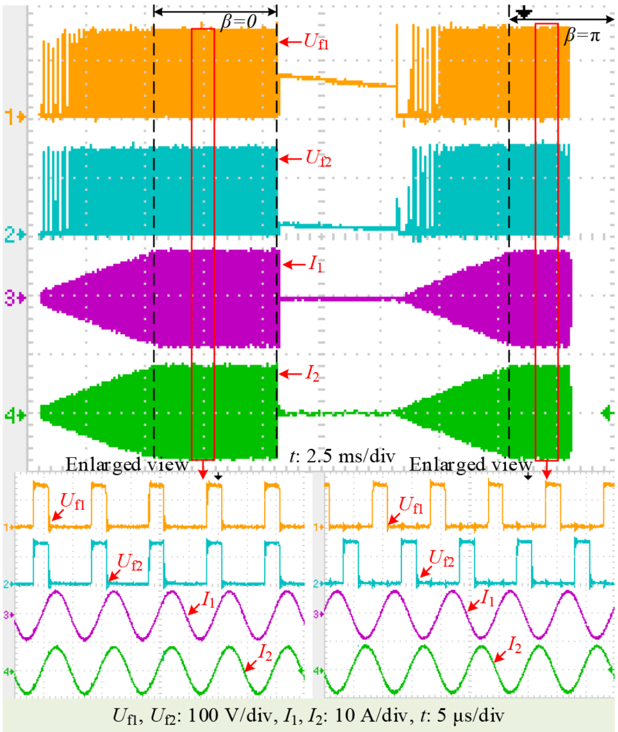

Fig. 18. Experimental waveforms during the phase difference scanning process.

The total weight of the two receiving coils is 293 g, which refers solely to the weight of the Litz wire used for winding, excluding the weight of the winding frame and the rectifier board. It is worth noting that the receiving coil was dimensionally designed with reference to the DJI Phantom 4-Pro. However, this UAV has a total weight of only 1388 g and exhibits very limited payload capacity. Consequently, the designed receiver is unsuitable for application on the DJI Phantom 4-Pro due to its relatively heavy weight. Nevertheless, the proposed magnetic coupler can serve as a valuable reference for wireless charging applications targeting UAVs with similar landing gear structures, such as the DJI T100 agricultural UAV, which boasts a payload capacity of 75 kg.

B. Phase Difference and Duty Cycle Scanning Results

Fig. 18 shows the experimental waveforms during the phase difference scanning process, where the two enlarged views represent the waveforms of the two inverters' output voltages and excitation currents when $\beta = 0$ and π, respectively. As shown in Fig. 18, when β is 0 and π, the two excitation currents remain in the same phase and reverse phase, respectively. In Fig. 18, there are two time periods corresponding to a slow increase in excitation currents, which is due to the gradual increase in the duty cycle of the two inverters from 0 to 0.25. In addition, there is a period in Fig. 18 corresponding to two excitation currents of 0, which is set to the shutdown state to avoid overshoot caused by directly switching from the same phase stage to the reverse phase stage. The entire phase difference scanning process takes a total of 25 ms.

Fig. 19 shows the experimental waveforms during the duty cycle scanning process. The duty cycles of the two inverters always maintain a complementary relationship, that is, α_1+α_2 = 0.5. The duty cycle of the Inverter-2 increases from 0 to 0.5, and the duty cycle of the Inverter-1 decreases from 0.5 to 0.

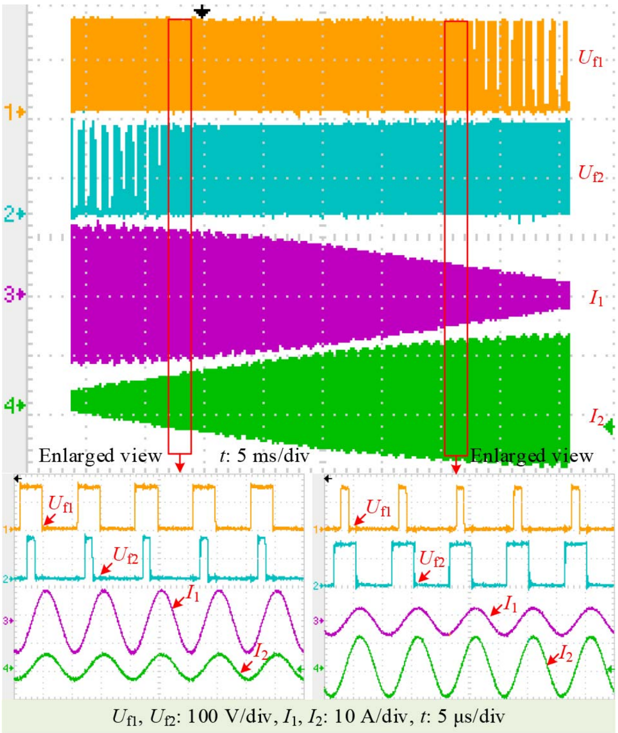

Fig. 19. Experimental waveforms during the duty cycle scanning process.

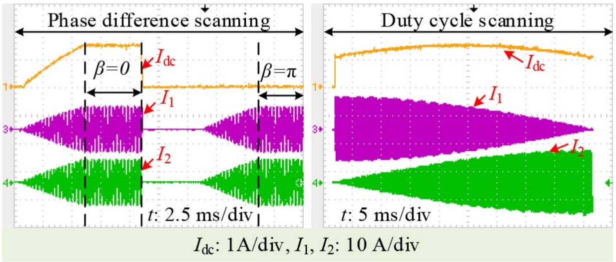

Fig. 20. Input current waveforms during the phase difference and duty cycle scanning process when $\theta = 45°$.

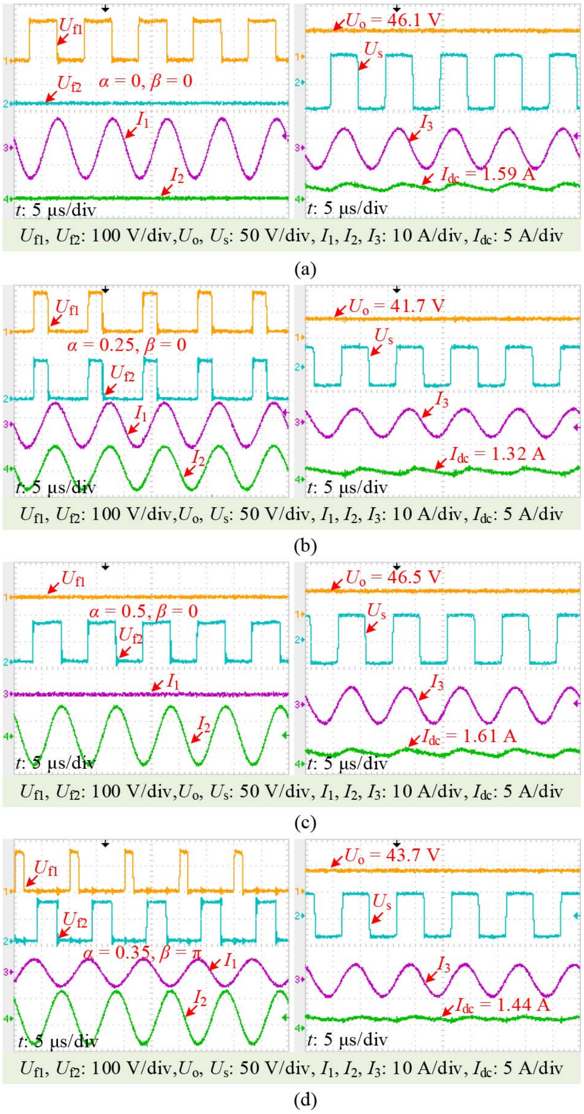

Fig. 21. Experimental steady-state waveforms at four angular misalignments. (a) $\theta = 0°$. (b) $\theta = 45°$. (c) $\theta = 90°$. (d) $\theta = 120°$.

The step size of the duty cycle change is 0.01, and it changes every 1 ms. The entire duty cycle scanning process takes a total of 50 ms. The essence of duty cycle scanning is the excitation current scanning. During the scanning process, one excitation current increases and the other excitation current decreases, as shown in Fig. 19.

When the receiver's angular misalignment θ is 45°, the recorded input current waveforms (see I_{dc}) during the phase difference and duty cycle scanning process are shown in Fig. 20. During the phase difference scanning process, when $\beta = 0$ and π, the detected I_{dc} is about 1.32 A and 0 A, respectively. The optimized value of β is 0 because 1.32 A $>$ 0 A, meaning that the two excitation currents need to remain in the same phase. During the duty cycle scanning process, I_{dc} first increases and then decreases. The maximum value of I_{dc} is about 1.32 A, corresponding to α of 0.25. Therefore, the optimal α obtained during the duty cycle scanning stage is 0.25.

The results of phase difference and duty cycle scanning in Fig. 20 are consistent with the simulation results in Fig. 12. Taking into account the waiting and soft start time, it takes a total of 85 ms to find the optimal α and β. The time taken for this scan is extremely short compared to the time required for wireless charging of the UAV.

This article selects four different angular misalignments ($\theta = 0°, 45°, 90°, 120°$) to analyze the results of phase difference and duty cycle scanning, where the definition of angular misalignment is shown in Fig. 4(c). Fig. 21 shows the experimental steady-state waveforms at four angular misalignments.

When $\theta = 0°$, the optimal values of α and β obtained by scanning are both 0. That is, Inverter-2 remains in the OFF state, while Inverter-1 operates at a duty cycle of 0.5, as shown in Fig. 21(a). The measured output voltage U_{o} and input current I_{dc} are 46.1 V and 1.59 A, respectively. Due to the constant load and input voltage during the experiment, which are 10 Ω and

TABLE III
THEORETICAL AND SCANNED VALUES OF THE DUTY CYCLE AND PHASE DIFFERENCE

θ	0°	45°	90°	120°
Measured M_{13} (μH)	9.71	6.27	0	−4.29
Measured M_{23} (μH)	0	6.34	9.82	8.33
Theoretical α	0	0.2518	0.5	0.3485
Theoretical β	0	0	0	π
Scanned α	0	0.25	0.5	0.35
Scanned β	0	0	0	π

150 V, respectively, the output power P_o and dc-to-dc efficiency η can be calculated to be 212.5 W and 89.1%, respectively.

When $\theta = 45°$, the optimal values of α and β are 0.25 and 0, respectively. That is, both inverters are operating at a duty cycle of 0.25 and remain in the same phase state, as shown in Fig. 21(b). The measured U_o and I_{dc} are 41.7 V and 1.32 A, respectively. P_o and η are 173.9 W and 87.8%, respectively.

When $\theta = 90°$, the optimal values of α and β are 0.5 and 0, respectively. That is, Inverter-1 remains in the OFF state, while Inverter-2 operates at a duty cycle of 0.5, as shown in Fig. 21(c). The measured U_o and I_{dc} are 46.5 V and 1.61 A, respectively. P_o and η are 216.2 W and 89.5%, respectively.

When $\theta = 120°$, the optimal values of α and β are 0.35 and π, respectively. That is, Inverter-1 and Inverter-2 operate in reverse phases with duty cycles of 0.15 and 0.35, respectively, as shown in Fig. 21(d). The measured U_o and I_{dc} are 43.7 V and 1.44 A, respectively. P_o and η are 191.0 W and 88.2%, respectively.

The theoretical basis for the scanning results in Fig. 21 is as follows: The power allocated to the two transmitters is mainly determined by their mutual inductances. If the mutual inductance is large, a larger power needs to be allocated, and the corresponding inverter needs to provide a larger duty cycle. If the signs of the two mutual inductances are different, the two excitation currents must be set to opposite phases to avoid the power picked up by each canceling out.

Table III presents the theoretical and scanned values of the duty cycle and phase difference. The values of M_{13} and M_{23} under four angular misalignment conditions are measured using an *LCR* meter. The theoretical values of α and β are calculated using (14), while their practical values are determined through experimental scanning. For all four angular misalignment cases, the theoretical and scanned values of β are identical. This is because the difference between the input currents corresponding to the same phase and reverse phase states of the two inverters is sufficiently large, making incorrect determination of β highly unlikely. Similarly, the theoretical and scanned values of α are identical when the receiver is at 0° and 90°. Under these specific angles, only one inverter is active while the other is shut down. When the system operates in single-inverter mode, the corresponding duty cycle is fixed at 0.5. However, minor discrepancies between the theoretical and scanned values of α are observed when the receiver is at 45° and 135°. These errors are attributed to the scanning step size of α (0.01). Overall, the theoretical and scanned values of α and β are in good agreement.

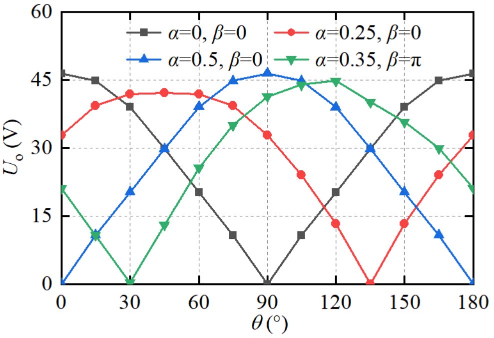

Fig. 22. Relationship between the output voltage U_o and the receiver's angular misalignment θ under four operating states of the system.

It is important to note that the scanning method proposed in this work differs from mutual inductance identification and intelligent optimization algorithms. Maximum efficiency tracking based on mutual inductance identification relies heavily on the accuracy of current sensing and mutual inductance estimation. Intelligent optimization algorithms, on the other hand, may converge to local optima rather than the global optimum. In contrast, the proposed method compares the relative magnitudes of the input currents to determine the optimal α and β. Although absolute errors may occur during current measurement, the relative comparison approach minimizes the probability of significant errors. Furthermore, the full-scanning strategy adopted in this work effectively avoids convergence to local optima.

C. *Targeting Magnetic Field Verification*

The previous section provided the optimal phase difference and duty cycle for four angular misalignments. This section will demonstrate whether the transmitter generates a targeting magnetic field when the system is operating under these four optimal α and β. Namely, verify whether the magnetic field generated by the transmitter is pointing vertically toward the receiver. It is difficult to directly measure the direction of the resultant magnetic field generated by the transmitter. Therefore, we will indirectly describe the direction of the resultant magnetic field by searching for the maximum output voltage under different angular misalignments. Fig. 22 shows the relationship between the output voltage U_o and the receiver's angular misalignment θ under four operating states of the system.

When $\theta = 0°$, from Fig. 21(a), the optimal values of α and β are both 0. Now, keep the system operating in a state where both α and β are 0, and change the receiver angle in steps of 15°. Then, measure the corresponding U_o at each angle as shown in the black curve in Fig. 22. When $\theta = 0°$, the corresponding U_o is the highest, with a value of 46.1 V. This measurement result indicates that the resultant magnetic field generated by the transmitter is along the positive *x*-axis direction, as shown in Fig. 23(a).

When $\theta = 45°$, from Fig. 21(b), the optimal values of α and β are 0.25 and 0, respectively. Now, keep the system operating in a state where $\alpha = 0.25$ and $\beta = 0$. The relationship between U_o and θ is shown by the red curve in Fig. 22. When $\theta = 45°$,

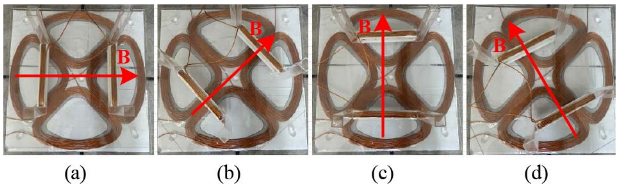

Fig. 23. Resultant magnetic field under four different angular misalignments. (a) $\theta = 0°$. (b) $\theta = 45°$. (c) $\theta = 90°$. (d) $\theta = 120°$.

the corresponding U_o is the highest, with a value of 41.7 V. This measurement result indicates that the resultant magnetic field generated by the transmitter is at a 45° angle to the x-axis direction, as shown in Fig. 23(b).

When $\theta = 90°$, from Fig. 21(c), the optimal values of α and β are 0.5 and 0, respectively. Now, keep the system operating in a state where $\alpha = 0.5$ and $\beta = 0$. The relationship between U_o and θ is shown by the blue curve in Fig. 22. When $\theta = 90°$, the corresponding U_o is the highest, with a value of 46.5 V. This measurement result indicates that the resultant magnetic field generated by the transmitter is at a 90° angle to the x-axis direction, as shown in Fig. 23(c).

When $\theta = 120°$, from Fig. 21(d), the optimal values of α and β are 0.35 and π, respectively. Now, keep the system operating in a state where $\alpha = 0.35$ and $\beta = \pi$. The relationship between U_o and θ is shown by the green curve in Fig. 22. When $\theta = 120°$, the corresponding U_o is the highest, with a value of 43.7 V. This measurement result indicates that the resultant magnetic field generated by the transmitter is at a 120° angle to the x-axis direction, as shown in Fig. 23(d).

The measurement results in Fig. 22 verify the correctness of generating targeted magnetic fields through phase difference and duty cycle scanning methods.

D. Omnidirectional Powering Results

Fig. 24 illustrates several typical test scenarios for evaluating angular and positional misalignments. Specifically, Fig. 24(a) shows rotation about the z-axis from 0° to 180° with no positional misalignment ($\Delta x = \Delta y = 0$ mm). Fig. 24(b) and (c) present the same rotational sweep under horizontal displacements of $\Delta x = 100$ mm and $\Delta y = 100$ mm, respectively. Fig. 24(d) and (e) demonstrate linear displacements along the x- and y-axes, each ranging from 0 to 100 mm. Finally, Fig. 24(f) depicts a combined case: the receiver is moved along the 45° direction by 0–100 mm while maintaining a 45° angular misalignment.

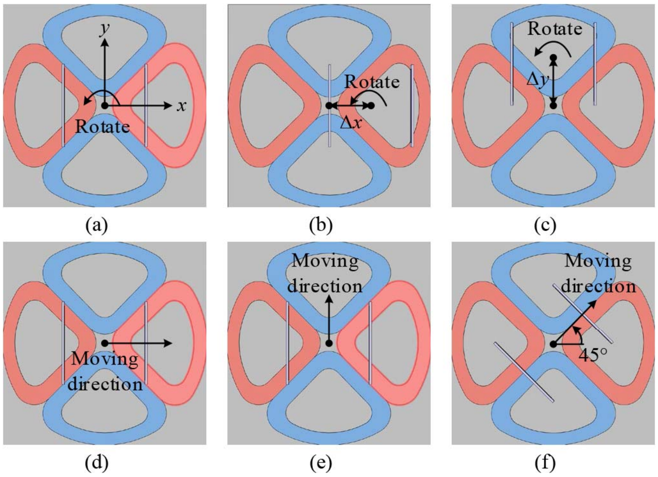

Fig. 24. Several typical cases for testing angular and positional misalignments. (a) Rotate when $\Delta x = \Delta y = 0$ mm. (b) Rotate when $\Delta x = 100$ mm. (c) Rotate when $\Delta y = 100$ mm. (d) x-directional misalignment. (e) y-directional misalignment. (f) 45°-directional misalignment.

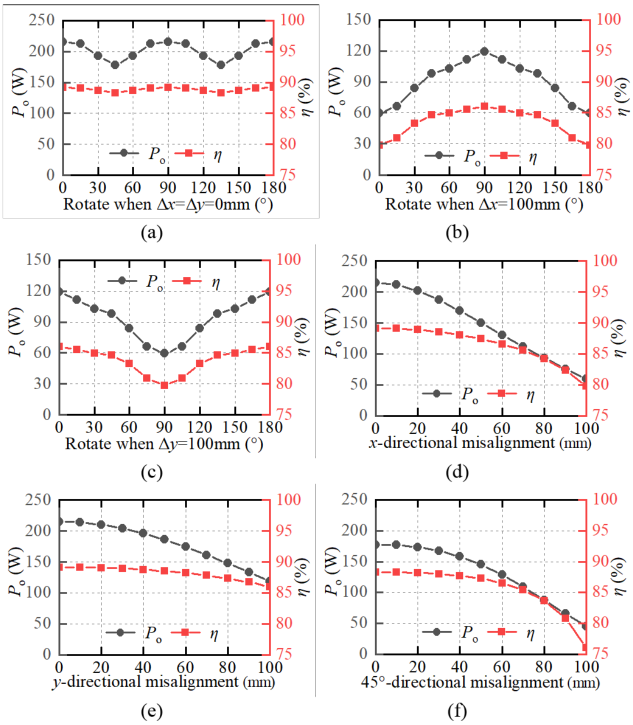

Fig. 25. Output power P_o and system DC-to-DC efficiency η under several angular and positional misalignments. (a) Rotate when $\Delta x = \Delta y = 0$ mm. (b) Rotate when $\Delta x = 100$ mm. (c) Rotate when $\Delta y = 100$ mm. (d) x-directional misalignment. (e) y-directional misalignment. (f) 45°-directional misalignment.

Fig. 25 shows the output power P_o and system dc-to-dc efficiency η under several angular and positional misalignments. When the receiver is rotated about the z-axis without positional misalignment, P_o remains in the range of 177.6–216.2 W, and η stays between 88.3% and 89.5%, as shown in Fig. 25(a). Both P_o and η reach their maximum values when the rotation angle is 0° or 90°. This occurs because, at these angles, only one coil is active while the other is turned OFF, thereby reducing system losses. A discussion on determining the single-coil operating mode to simplify the control strategy will be provided in Section VI. Both P_o and η reach their minimum values when the rotation angle is 45° or 135°. When the receiver is rotated about the z-axis at $\Delta x = 100$ mm and $\Delta y = 100$ mm, the measured P_o and η are shown in Fig. 25(b) and (c), respectively. P_o remains within the range of 59.4–119.1 W, while η varies from 79.7% to 86.0%.

From Fig. 25(d), when the receiver is offset by 100 mm in the x-direction, P_o decreases to 59.4 W and η decreases to 79.7%. From Fig. 25(e), when the receiver is offset by 100 mm in

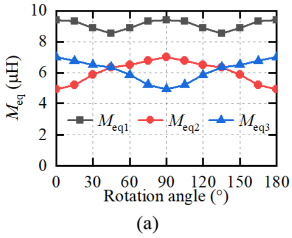

Fig. 26. Relationship of equivalent mutual inductance $M_{\rm eq}$ with (a) rotation angle and (b) offset distance.

the y-direction, $P_{\rm o}$ decreases to 119.1 W and η decreases to 86.1%. From Fig. 25(f), when the receiver is offset by 100 mm in the 45°-direction, $P_{\rm o}$ decreases to 44.6 W and η decreases to 76.1%. Based on the above analysis, the maximum output power and dc-to-dc efficiency of the system are 216.2 W and 89.5%, respectively. The dc-to-dc efficiency exceeds 76.1% across ±100 mm positional misalignment and arbitrary angular misalignment.

The attenuation of output power and efficiency with misalignment, as shown in Fig. 25, can be characterized by the mutual inductance. Based on the output power calculation formula given in (12), the equivalent mutual inductance between the transmitter and receiver is defined as $M_{\rm eq} = \sqrt{M_{12}^2 + M_{13}^2}$. The mutual inductances M_{12} and M_{13} under the six misalignment conditions illustrated in Fig. 24 can be obtained through simulation. Let $M_{\rm eq1}$, $M_{\rm eq2}$, and $M_{\rm eq3}$ denote the equivalent mutual inductances corresponding to the three angular misalignments shown in Fig. 24(a), (b), and (c), respectively. Similarly, let $M_{\rm eq4}$, $M_{\rm eq5}$, and $M_{\rm eq6}$ represent the equivalent mutual inductances for the three positional misalignments in Fig. 24(d), (e), and (f). The relationship of equivalent mutual inductance with rotation angle and offset distance is presented in Fig. 26.

In Fig. 26(a), since $M_{\rm eq1}$ is larger and more stable than $M_{\rm eq2}$ and $M_{\rm eq3}$, the angular misalignment tolerance in Fig. 25(a) is better than that in Fig. 25(b) and (c). In Fig. 26(b), as the offset distance increases, $M_{\rm eq5}$ decreases at the slowest rate, followed by $M_{\rm eq4}$, while $M_{\rm eq6}$ decreases the fastest. Therefore, the configuration in Fig. 25(e) exhibits the best positional misalignment tolerance, Fig. 25(d) ranks second, and Fig. 25(f) shows the poorest performance in resisting positional misalignment.

When the system is operating at maximum power, the measured values of I_1, I_2, and I_3 are 0 A, 7.16 A, and 5.15 A, respectively, and the phase difference between I_3 and I_2 is 90°. By inputting the above currents into the COMSOL simulation calculation, the magnetic flux density distribution on a cross section at the maximum power transfer is obtained as shown in Fig. 27. The main magnetic flux is concentrated in the receiver, with almost no magnetic flux passing through the UAV. This is because the bipolar transmitting coil mainly generates a horizontal magnetic field rather than a vertical magnetic field. Therefore, the proposed magnetic coupler has the advantage of low leakage flux interference.

E. Comparison With Rotating Magnetic Field

Generally, a higher magnetic field utilization rate implies higher transmission efficiency. Since magnetic field utilization rate is not easily quantified, this article compares the targeting magnetic field mode with the rotating magnetic field mode from the perspective of transmission efficiency. According to Ref. [19], a rotating magnetic field can be generated by exciting two orthogonal coils with currents of equal amplitude and a phase difference of 90°. Therefore, in the proposed UAV-WPT system, a rotating magnetic field is produced by maintaining the duty cycles of both inverters at 0.5 and their phase difference at 90°, while keeping all other parameters (including input voltage, operating frequency, and compensation networks) unchanged. The measured dc-to-dc efficiencies of both the targeting and rotating magnetic field modes are shown in Fig. 28.

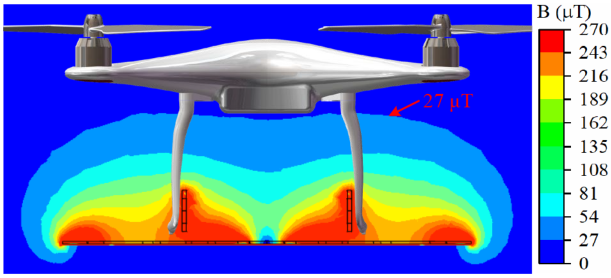

Fig. 27. Magnetic flux density distribution on a cross section at the maximum power transfer.

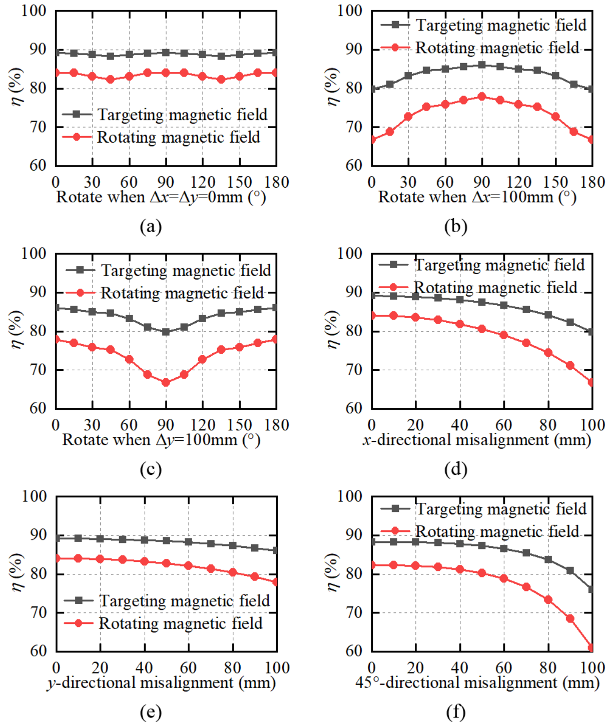

Fig. 28. DC-to-DC efficiency η comparison between targeting magnetic field and rotating magnetic field modes under several angular and positional misalignments. (a) Rotate when $\Delta x = \Delta y = 0$ mm. (b) Rotate when $\Delta x = 100$ mm. (c) Rotate when $\Delta y = 100$ mm. (d) x-directional misalignment. (e) y-directional misalignment. (f) 45°-directional misalignment.

Under various angular and positional misalignments, the targeting magnetic field mode consistently demonstrates higher efficiency than the rotating magnetic field mode. When the receiver has no misalignment, the efficiencies of the targeting and rotating

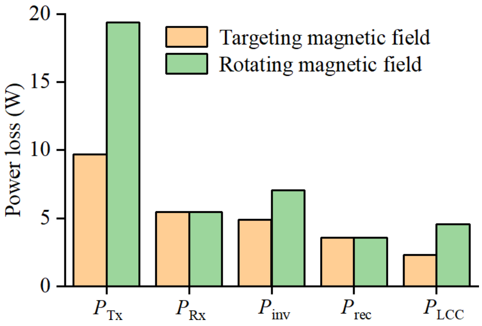

Fig. 29. Power loss comparison between targeting magnetic field and rotating magnetic field modes.

magnetic field modes are 89.1% and 84.1%, respectively, with a minimum difference of 5%. When the receiver is displaced by 100 mm along the 45° direction, the corresponding efficiencies are 76.1% and 60.9%, resulting in a maximum difference of 15.2%. In summary, the dc-to-dc efficiency of the targeting magnetic field mode is at least 5% higher than that of the rotating magnetic field mode.

Fig. 29 shows the power loss comparison between targeting magnetic field and rotating magnetic field modes when no misalignment occurs. P_{Tx}, P_{Rx}, P_{inv}, P_{rec}, and P_{LCC} represent the total power losses of the two transmitting coils, the combined losses receiving coil and its series compensation capacitors, the total losses of the two inverters, the loss of the rectifier, and the total losses of the two *LCC* compensation networks, respectively. The P_{Tx}, P_{Rx}, and P_{LCC} can be calculated from the ESR and current of the component. The P_{inv} and P_{rec} can be calculated according to [23].

In targeting magnetic field mode, the output power, total power loss, and dc-to-dc efficiency are 212.5 W, 26 W, and 89.1%, respectively. The values of P_{Tx}, P_{Rx}, P_{inv}, P_{rec}, and P_{LCC} are 9.7, 5.5, 4.9, 3.6, and 2.3 W, respectively. In rotating magnetic field mode, the output power, total power loss, and dc-to-dc efficiency are 212.5 W, 40.2 W, and 84.1%, respectively. The values of P_{Tx}, P_{Rx}, P_{inv}, P_{rec}, and P_{LCC} are 19.4, 5.5, 7.1, 3.6, and 4.6 W, respectively. When the receiver has no misalignment, the mutual inductance between Coil-2 and the receiver is nearly zero, so Coil-2 cannot deliver power to the receiver. In targeting magnetic field mode, only Inverter-1 and Coil-1 are active, while Inverter-2 and Coil-2 are turned OFF. In rotating magnetic field mode, both inverters remain operational, with both excitation currents maintained at their rated values. As a result, P_{Tx}, P_{inv}, and P_{LCC} in targeting magnetic field mode are all lower than those in rotating magnetic field mode.

F. Comparison With Previous Works

Table IV shows the comparison with typical UAV-WPT systems. Ref. [6] exemplifies face-to-face magnetic couplers, offering structural simplicity and superior angular misalignment tolerance. However, these transmitters generate a vertically (*z*-direction) magnetic field, causing significant flux penetration through UAV airframes and consequent leakage flux interference. In addition, receiver deployment compromises the UAV's original aerodynamic profile, which is not conformal. Ref. [12] is a representative of using a horizontal (*x*-direction) magnetic field to transfer power, which minimizes leakage flux interference but exhibits poor angular misalignment tolerance. Ref. [16] is a typical simple scheme that does not rely on magnetic field control and only designs the magnetic coupler to improve angular misalignment tolerance. This type of transmitter generates a magnetic field in all directions (omnidirectional) on a 2-D plane. However, the receiver usually only requires a specific direction of magnetic field after a UAV completes its landing, and most of the magnetic field cannot be utilized, resulting in a low magnetic field utilization rate. Ref. [19] is a representative of using a 2-D rotating magnetic field to achieve omnidirectional powering. Such a method has the advantages of not requiring receiver angle detection and being simple to implement. Nevertheless, it suffers from low magnetic field utilization rate since the generated flux remains nonperpendicular to the receiving coil during most scanning cycles.

Both Ref. [4] and this article employ active magnetic field control to achieve a targeting magnetic field, ensuring the magnetic field generated by the transmitter is always perpendicular to the receiving coil, thereby achieving a significantly higher magnetic field utilization rate. The key to generating a targeting magnetic field lies in determining the receiver's attitude. Ref. [4] utilizes mutual inductance identification to estimate the receiver's attitude indirectly. However, this method requires prior knowledge of the load value. In practical applications, additional load identification is necessary, which increases the complexity of system implementation. In contrast, this article adopts a phase difference and duty cycle scanning approach to identify the combination that corresponds to the maximum dc input current, thereby achieving targeting magnetic fields more simply.

The primary reason for the relatively heavy weight of the receiving coil is the use of a thick litz wire, specified as 0.05 mm × 1300 strands, with a rated current of 10.2 A. However, the maximum current in the receiving coil under actual operating conditions is only 5.15 A. Therefore, a litz wire with a specification of 0.05 mm × 650 strands would be sufficient in practical applications. If such a wire is used, the weight of the receiving coil can be reduced to approximately 146 g. Note that the weight mentioned refers to the total weight of the receiving coils installed on both sides of the UAV landing gear. The lower weight of the receiving coil in Ref. [19] is attributed to the use of only one receiving coil mounted on the UAV landing gear. However, this configuration may lead to an imbalance in weight between the left and right sides of the landing gear.

The weight of the receiving coil is not only related to the transmitted power but is also significantly influenced by the air gap of the coupler. A smaller air gap requires fewer turns of the receiving coil to meet the power requirements, thereby reducing weight. In this study, considering the practical need for a certain thickness in encapsulating the transmitter and receiver, the air gap was set to 20 mm. This air gap is larger than those used in other studies, which contributes to the increased weight of the receiving coil. The operating frequency in this work is 100 kHz. Future research could explore higher operating frequencies to further reduce the weight of the receiving coil.

TABLE IV
COMPARISON WITH TYPICAL UAV-WPT SYSTEMS

Ref.	[6]	[12]	[16]	[19]	[4]	This article
Magnetic field distribution	*z*-direction	*x*-direction	Omnidirectional in a 2-D plane	Rotating magnetic field	Targeting magnetic field	Targeting magnetic field
Control method	No control	No control	No control	90° phase difference	Mutual inductance identification	Phase difference and duty cycle scanning
Control difficulty	Simple	Simple	Simple	Simple	Difficult	Moderate
Magnetic field utilization rate	Moderate	Moderate	Low	Low	High	High
Leakage flux interference	High	Low	Low	Low	Low	Low
Conformal	No	Yes	Yes	Yes	Yes	Yes
Angular misalignment	0–360°	0–45°	0–360°	0–360°	0–360°	0–360°
Positional misalignment	75 mm	20 mm	20 mm	50 mm	60 mm	100 mm
Maximum power	13 W	87.4 W	113.6 W	300.6 W	176 W	216.2 W
Maximum efficiency	60%	87.3%	88.6%	88.9%	86.1 %	89.5%
Coupler's gap	/	15 mm	10 mm	10 mm	0 mm	20 mm
Receiver's weight	/	56.4 g	/	105 g	150 g	293 g

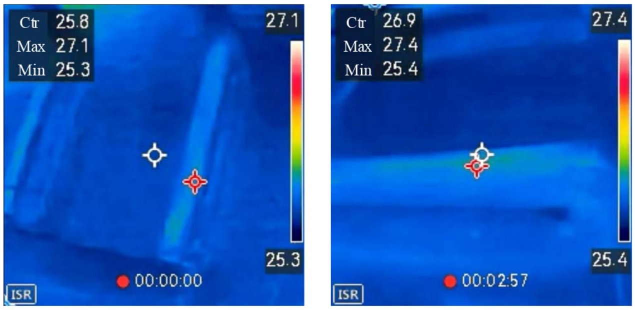

(a) (b)

Fig. 30. Relationship between receiving coil temperature and time: (a) time = 0 and (b) time = 2 min 57 s.

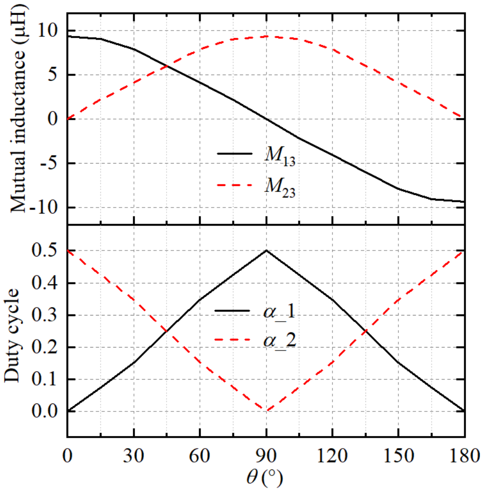

Fig. 31. Simulated mutual inductance versus the theoretical optimal duty cycle under different angular misalignment.

Fig. 30 shows the temperature variation of the receiving coil over time when the system operates without misalignment. At time = 0, the coil temperature is 27.1°C; at time = 2 min 57 s, the coil temperature reaches 27.4°C. The coil exhibits negligible temperature rise. This can be attributed to two main factors: first, the system operates at a relatively low output power of 216.2 W, and the total power loss of the two receiving coils is only 5.5 W; Second, the receiving coil is not encapsulated, allowing it to dissipate heat effectively through direct contact with the air.

Regarding the overall weight optimization of the receiver side, which includes the receiving coil, compensation network, rectifier circuit, and the dc-dc converter required for practical charging. Using thinner wires, reducing the number of capacitors in the compensation array, optimizing component layout for higher density, and employing smaller heat sinks could all contribute to weight reduction. However, these modifications may lead to significant temperature rise, potentially affecting system longevity. Therefore, careful consideration of thermal management strategies is essential when implementing weight optimization measures.

VI. DISCUSSION ON CONTROL STRATEGY

Fig. 31 shows the simulated mutual inductance versus the theoretical optimal duty cycle under different angular misalignment θ. When $\theta = 0°$, M_{23} equals zero. At this point, Coil-2 cannot transfer power to the receiver. Therefore, Inverter-2 and Coil-2 are shut down to reduce losses. Similarly, when $\theta = 90°$, M_{13} equals zero. Under this condition, Coil-1 cannot supply power to the receiver, so Inverter-1 and Coil-1 are turned OFF to minimize

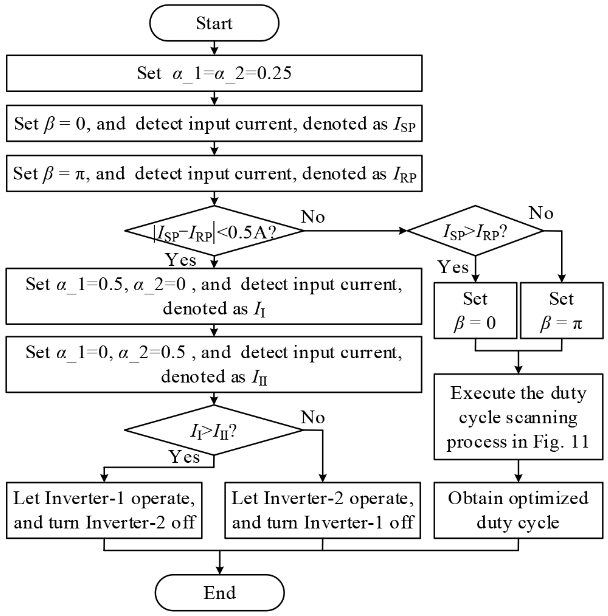

Fig. 32. Flowchart for determining single or dual-coil operation.

losses. When $\theta < 15°$, M_{13} is significantly larger than M_{23}, and the theoretical optimal duty cycle of α_2 is less than 0.1. In this case, the power provided by Inverter-2 is very limited. Experimental results indicate that operating with only one coil yields higher efficiency than using both coils simultaneously. Hence, when θ is within the range of $(-15°, 15°)$, Inverter-2 can remain shut down to reduce losses. Similarly, when θ is between 75° and 105°, M_{23} is much greater than M_{13}, and the theoretical optimal duty cycle of α_1 falls below 0.1. At this point, since the power supplied by Inverter-1 is negligible, it can be kept deactivated to avoid unnecessary losses. Thus, introducing a single-coil operation mode judgment can help simplify the control strategy.

Fig. 32 shows the flowchart for determining single or dual-coil operation. Since the angular misalignment of the receiver is unknown, the system indirectly determines the operating mode by measuring the dc input current. When θ falls within the ranges of $(-15°, 15°)$ or $(75°, 105°)$, one transmitter coil exhibits strong coupling with the receiving coil, while the other shows very weak coupling. Therefore, both inverters are first set to a duty cycle of 0.25 and operated in the same phase and reverse phase, respectively. The corresponding dc input currents are measured and denoted as I_{SP} and I_{RP}. If the difference between I_{SP} and I_{RP} is small (with a simulation-derived threshold of 0.5 A), it is concluded that one transmitter coil is weakly coupled and cannot deliver sufficient power. Thus, the system switches to single-coil operation. Each inverter is then activated alternately while monitoring the corresponding dc input current to determine which coil should remain active. If the difference between I_{SP} and I_{RP} exceeds 0.5 A, both transmitting coils are considered capable of supplying considerable power to the receiver, and the system operates in dual-coil mode. The duty cycle scanning method shown in Fig. 11 is then applied to identify the optimal duty cycle. Fig. 32 reduces the computational burden by decreasing the probability of executing duty cycle scanning. It is worth noting that although single-coil operation achieves higher efficiency than dual-coil operation, using only one coil is insufficient when θ is outside the $(-15°, 15°)$ and $(75°, 105°)$ ranges. In such cases, both coils must operate simultaneously to meet the power requirements.

The primary reason for adopting a linear scanning approach to determine the optimal duty cycle and phase difference in this study is its simplicity and reliability. Only two-phase difference scans are required to determine whether the optimal phase difference is 0° or 180°. Similarly, finding the optimal duty cycle necessitates only 50 scanning steps. The entire process of identifying the optimal phase difference and duty cycle takes only 82 ms. Although the system employs two inverters driving two coils, the duty cycles of the two inverters maintain a complementary relationship. As a result, there is effectively only one control variable. In contrast, traditional magnetic field vector synthesis control methods with two or three coils generally involve two or three control variables, respectively. For a system with two control variables, if the same scanning step size is applied, a total of $50 \times 50 = 2500$ scanning steps would be required. In the case of three control variables, this number increases drastically to 125 000 steps. Therefore, applying the linear scanning method to systems with multiple control variables is impractical. Alternative approaches, such as mutual inductance identification or more advanced optimization algorithms, should be considered.

The optimal excitation current amplitudes for multiple transmitting coils primarily depend on the mutual inductance between each transmitting and the receiving coil. Once the mutual inductance values are identified, the optimal excitation currents can be derived analytically [4]. However, mutual inductance identification among multiple coils requires determining not only the magnitude but also the sign of the mutual inductance, which complicates the implementation. Furthermore, most existing mutual inductance identification methods assume that the load value is known, while in practice, the load is often unknown and time-varying [24].

Common optimization algorithms, such as genetic algorithms, particle swarm optimization, and simulated annealing, are suitable for complex problems with large search spaces. However, due to their high computational complexity, these methods are often impractical for implementation on embedded controllers, such as STM32 or DSPs [25]. Gradient descent and invasive weed optimization algorithms represent alternative optimization schemes. These are more suitable for scenarios where the receiver's position and orientation change frequently [26], [27]. In future work, we will explore multidegree-of-freedom wireless charging for hovering UAVs. Given the presence of hovering disturbances, which may cause frequent changes in position and angle, advanced gradient descent-based optimization could be a promising solution. For wireless charging of landed UAVs, where position and angle generally remain unchanged, the simple linear scanning method remains sufficient and effective.

VII. CONCLUSION

To address the issue of misalignment tolerance and magnetic field utilization rate for a UAV-WPT system, a transmitter with two orthogonal bipolar coils and its targeting magnetic field control method are proposed. The two transmitting coils predominantly generate x-directional and y-directional magnetic fields, respectively. Through magnetic field vector superposition, the resultant magnetic field generated by the transmitter can always be directed perpendicular to the receiving coil plane by regulating excitation current amplitude and phase in both coils, thus forming a targeting magnetic field. The mapping relationship between required excitation currents and receiver angles is analytically derived. Excitation current amplitude and phase difference are controlled via duty cycle and phase difference adjustments in dual half-bridge inverters. To avoid detecting receiver angle directly, the generation of a targeting magnetic field is implemented from a maximum efficiency transmission perspective. Theoretical analysis indicates that under the same duty cycle and phase difference parameters, the output power, transmission efficiency, and input power can reach their maximum values simultaneously. Consequently, a targeting magnetic field control method integrating duty cycle and phase difference scanning with dc input current detection is developed. Experimental results indicate that the system establishes a targeting magnetic field within 85 ms, delivering a maximum output power of 216.2 W and a peak dc–to-dc efficiency of 89.5%. It maintains an efficiency above 76.1% under positional misalignments of up to ±100 mm and arbitrary angular misalignments. Notably, the targeting field mode exhibits at least a 5% higher dc–to-dc efficiency than the rotating field mode.

The key advantages of the proposed system are as follows:

1) The two orthogonal bipolar coil configurations with a targeting field control achieves omnidirectional powering and superior field utilization rate simultaneously.
2) The control method requires only transmitter-side dc input current detection, eliminating mutual inductance identification, receiver attitude detection, and communication links.
3) An orthogonal transmitting coil arrangement enables independent control of two excitation currents due to inherent decoupling.
4) Receiving coils maintain coplanarity with the landing gear, ensuring aerodynamic conformity.
5) The horizontal magnetic field generated by the transmitter can reduce the magnetic flux leakage interference passing through the UAV.

It is worth mentioning that the proposed dual-coil system incorporates one additional inverter and an *LCC* resonant network compared to a single-coil system, resulting in increased hardware complexity and cost. However, the proposed system significantly improves tolerance to both positional and angular misalignments while enhancing power transfer efficiency. This trade-off is worthwhile for applications such as UAV wireless charging, where high misalignment tolerance and transmission efficiency are critical requirements.

REFERENCES

[1] X. Lv et al., “A high misalignment tolerance SCC-WPT system with relay single capacitive coupler for UAV wireless charging applications,” *IEEE Trans. Power Electron.*, vol. 40, no. 8, pp. 10372–10377, Aug. 2025.

[2] M. Liao et al., “UAV fleet charging on telecom towers with differential capacitive wireless power transfer,” *IEEE Trans. Power Electron.*, vol. 40, no. 4, pp. 6370–6384, Apr. 2025.

[3] C. Cai et al., “Multi-state voltage balancing of UAV’s cell string: A reconfigurable WPT based multiport hybrid charging approach,” *IEEE Trans. Ind. Electron.*, vol. 72, no. 1, pp. 266–277, Jan. 2025.

[4] T. Feng, K. Shi, J. Jiang, and P. Wang, “A solenoid magnetic coupler and its control method for omnidirectional wireless charging of UAVs,” *IEEE Trans. Ind. Electron.*, vol. 72, no. 3, pp. 2540–2550, Mar. 2025.

[5] Y. Guan, Y. Qiao, J. Mai, Y. Wang, and D. Xu, “Compensation parameter optimization of inductive wireless power transfer system for low stray magnetic field,” *IEEE Trans. Power Electron.*, vol. 40, no. 5, pp. 7537–7548, May 2025.

[6] J. M. Arteaga, S. Aldhaher, G. Kkelis, C. Kwan, D. C. Yates, and P. D. Mitcheson, “Dynamic capabilities of multi-MHz inductive power transfer systems demonstrated with batteryless drones,” *IEEE Trans. Power Electron.*, vol. 34, no. 6, pp. 5093–5104, Jun. 2019.

[7] M. Xue, Y. Guo, W. Xu, Y. Gao, and S. Qiu, “Design and optimization of wide-coupling nested magnetic coupling mechanism for UAV wireless power transfer,” *IEEE Trans. Power Electron.*, vol. 40, no. 8, pp. 11849–11862, Aug. 2025.

[8] Y. Gu, J. Wang, Z. Liang, and Z. Zhang, “Communication-free power control algorithm for drone wireless in-flight charging under dual-disturbance of mutual inductance and load,” *IEEE Trans. Ind. Inform.*, vol. 20, no. 3, pp. 3703–3714, Mar. 2024.

[9] J. Wang, R. Chen, C. Cai, J. Zhang, and C. Wang, “An onboard magnetic integration-based WPT system for UAV misalignment-tolerant charging with constant current output,” *IEEE Trans. Transp. Electrific.*, vol. 9, no. 1, pp. 1973–1984, Mar. 2023.

[10] C. Rong et al., “Optimization design of resonance coils with high misalignment tolerance for drone wireless charging based on genetic algorithm,” *IEEE Trans. Ind. Appl.*, vol. 58, no. 1, pp. 1242–1253, Jan./Feb. 2022.

[11] C. Song et al., “EMI reduction methods in wireless power transfer system for drone electrical charger using tightly coupled three-phase resonant magnetic field,” *IEEE Trans. Ind. Electron.*, vol. 65, no. 9, pp. 6839–6849, Sep. 2018.

[12] S. Wu, C. Cai, L. Jiang, J. Li, and S. Yang, “Unmanned aerial vehicle wireless charging system with orthogonal magnetic structure and position correction aid device,” *IEEE Trans. Power Electron.*, vol. 36, no. 7, pp. 7564–7575, Jul. 2021.

[13] W. Chai, H. Zhang, S. Wu, and C. Cai, “Design of two orthogonal transmitters with double L-type ferrite for the wireless charging system in unmanned aerial vehicles,” *IEEE Trans. Transp. Electrific.*, vol. 9, no. 1, pp. 1985–1992, Mar. 2023.

[14] S. Wu, C. Cai, X. Liu, W. Chai, and S. Yang, “Compact and free-positioning omnidirectional wireless power transfer system for unmanned aerial vehicle charging applications,” *IEEE Trans. Power Electron.*, vol. 37, no. 8, pp. 8790–8794, Aug. 2022.

[15] Z. Bie, J. Zhang, K. Song, D. Wang, and C. Zhu, “A free-rotation asymmetric magnetic coupling structure of UAV wireless charging platform with conformal pickup,” *IEEE Trans. Ind. Electron.*, vol. 69, no. 10, pp. 10154–10161, Oct. 2022.

[16] Y. Li et al., “A new magnetic coupler with high rotational misalignment tolerance for unmanned aerial vehicles wireless charging,” *IEEE Trans. Power Electron.*, vol. 37, no. 11, pp. 12986–12991, Nov. 2022.

[17] P. Cao et al., “Embedded lightweight squirrel-cage receiving coil for drone misalignment-tolerant wireless charging,” *IEEE Trans. Power Electron.*, vol. 38, no. 3, pp. 2884–2888, Mar. 2023.

[18] W. Huang, Y. Zhang, F. Gao, and Y. Yang, “Magnetic structure design of wireless power transfer for free-rotating UAV with low stray magnetic fields,” *IEEE Trans. Ind. Electron.*, vol. 72, no. 1, pp. 481–491, Jan. 2025.

[19] C. Cai, D. Shen, S. Wu, X. Liu, and W. Chai, “A high misalignment tolerance IPT system for unmanned aerial vehicles based on multiwinding combined coupling,” *IEEE Trans. Transp. Electrific.*, vol. 10, no. 4, pp. 8566–8574, Dec. 2024.

[20] S. Wu, C. Cai, H. Zhang, X. Liu, and W. Chai, “A free-positioning IPT system via reconfigurable coil array transmitter for unmanned aerial vehicle applications,” *IEEE Trans. Transp. Electrific.*, vol. 10, no. 4, pp. 8746–8757, Dec. 2024.

[21] C. Zhang et al., “A strong misalignment-tolerance wireless power transfer system based on dynamic diffusion magnetic field for unmanned aerial vehicle applications,” *IEEE Trans. Power Electron.*, vol. 39, no. 11, pp. 14129–14134, Nov. 2024.

[22] C. Cai, J. Yang, S. Wu, H. Zhang, and W. Chai, “Landing position detection and array coil matching of multi-UAVs wireless power transfer system,” *IEEE Trans. Transp. Electrific.*, vol. 11, no. 5, pp. 11054–11064, Oct. 2025.

[23] B. X. Nguyen et al., “An efficiency optimization scheme for bidirectional inductive power transfer systems,” *IEEE Trans. Power Electron.*, vol. 30, no. 11, pp. 6310–6319, Nov. 2015.

[24] Z. Chen, X. Sun, J. Liu, Y. Yan, J. Zhao, and B. Ren, “Output power control strategy for omnidirectional wireless power transfer system based on maximum mutual inductance information estimation,” *IEEE J. Emerg. Sel. Topics Power Electron.*, vol. 12, no. 5, pp. 5383–5395, Oct. 2024.

[25] Z. Chen, X. Sun, W. Song, P. Wheeler, J. Liu, and B. Ren, “Maximum efficiency tracking control for omnidirectional wireless power transfer system based on AdamW algorithm,” *IEEE Trans. Power Electron.*, vol. 40, no. 3, pp. 4602–4612, Mar. 2025.

[26] Z. Yan et al., “Efficiency optimization of omnidirectional multiload wireless power transfer system based on magnetic vector regulation,” *IEEE J. Emerg. Sel. Topics Power Electron.*, vol. 13, no. 1, pp. 1361–1374, Feb. 2025.

[27] Z. Chen, X. Sun, J. Liu, B. Ren, and Z. Wang, “Research on maximum power point tracking control in omnidirectional wireless power transfer system,” *IEEE Trans. Ind. Electron.*, vol. 71, no. 7, pp. 6612–6621, Jul. 2024.

Tianxu Feng (Member, IEEE) received the B.E. degree in automation and the Ph.D. degree in control theory and control engineering from the School of Automation, Chongqing University, Chongqing, China, in 2016, and 2022, respectively. He is currently an Associate Professor with the School of Automation, Chongqing University of Posts and Telecommunications, Chongqing, China. His current research interests include wireless power transfer and power electronics.

Yuxuan Xu received the B.E. degree in automation in 2022 from the School of Automation, Chongqing University of Posts and Telecommunications, Chongqing, China, where he is currently working toward the M.S. degree in control engineering. His current research interests include wireless power transfer for uncrewed aerial vehicle.

Jincheng Jiang received the Ph.D. degree in control theory and control engineering from the School of Automation, Chongqing University, Chongqing, China, in 2020. He is currently a Lecturer with the School of Automation, Chongqing University of Posts and Telecommunications, Chongqing. His research interests include wireless power transfer technology and industrial IoT technology.

Ke Shi (Member, IEEE) received the B.E. degree in automation and the Ph.D. degree in control theory and control engineering from the School of Automation, Chongqing University, Chongqing, China, in 2016, and 2022, respectively. He is currently a Lecturer with the School of Automation, Chongqing University of Posts and Telecommunications, Chongqing. His current research interests include wireless power transfer and power electronics, dynamic wireless charging systems, and magnetic integrated methods.

Peiyue Wang received the B.E. degree in automation from Xidian University, Xi’an, China, in 2015, and the Ph.D. degree in control theory and engineering from Chongqing University, Chongqing, China, in 2021. He is currently a Lecturer with the School of Automation, Chongqing University of Posts and Telecommunications, Chongqing. His current research interests include wireless power transfer and power electronics.

Jie Hou (Member, IEEE) received the B.Eng. degree in automation from North Minzu University, Yinchuan, China, in 2010, the M.Eng. degree in control science and engineering from Chongqing University, Chongqing, China, in 2013, and the Ph.D. degree in control theory and control engineering from the Dalian University of Technology, Dalian, China, in 2018. From 2018 to 2021, he was a Lecturer with the Chongqing University of Posts and Telecommunications, Chongqing, where he is currently an Associate Professor. His current research interests include system identification and modeling.